Suspension thermal spraying of hydroxyapatite: Microstructure and *in vitro* behaviour

Giovanni Bolelli [a,*], Devis Bellucci [a], Valeria Cannillo [a], Luca Lusvarghi [a], Antonella Sola [a], Nico Stiegler [b], Philipp Müller [b], Andreas Killinger [b], Rainer Gadow [b], Lina Altomare [c], Luigi De Nardo [c]

[a] *Department of Engineering "Enzo Ferrari", Università di Modena e Reggio Emilia, Via Vignolese 905, 41125 Modena, MO, Italy*
[b] *Institute for Manufacturing Technologies of Ceramic Components and Composites (IMTCCC), Universität Stuttgart, Allmandring 7b, 70569 Stuttgart, Germany*
[c] *Dipartimento di Chimica, Materiali e Ingegneria Chimica "G. Natta", Politecnico di Milano, Via Mancinelli 7, I-20131 Milano, Italy*

Received 2 May 2013
Received in revised form 2 August 2013
Accepted 18 September 2013
Available online 27 September 2013

1. Introduction

In both dental and orthopaedic prostheses, cementless fixation to bone is gaining increasingly wide acceptance [1,2]. In cementless fixation, long-term stability depends on direct bony ingrowth into the surface of the implant [3], avoiding its undesirable encapsulation by fibrous tissue. In order to promote such ingrowth, the surface can be coated with an osteoconductive layer, which permits direct attachment and proliferation of bone tissue [4]. Of the available osteoconductive materials, hydroxyapatite (HA), with chemical formula $Ca_{10}(PO_4)_6(OH)_2$, is the most widely used for prosthetic coatings [5], and its preferred deposition method is plasma-spraying [6], on account of its versatility, relatively low cost, and short processing time. The deposition of TiO_2-based photocatalytic coatings with antibacterial properties is also possible [7,8].

Very high survival rates are reported [5,9–16] for HA-coated femoral stems in total hip replacement (THR) arthroplasty, usually superior to those for cemented or uncoated cementless stems. Good load transfer between the stem and the attached bone has been observed, with little stress shielding [9,11,16–19]. HA coatings have also been claimed to provide improved performance in dental implants [20,21], tibial components for total knee arthroplasty [22–25], and external fracture fixation pins [26].

It has been stressed that positive long-term implant fixation also requires proper mechanical interlocking between the implant surface and the ingrown bone: the former often has design features to encourage this, like tapered geometry, macroscopic grooves [27], threads [17,18], porous coatings (Ti beads or Ti fibermesh sintered onto the implant surface, or porous Ti layers by vacuum plasma-spraying [19,23]), or roughened surfaces (grit-blasted and/or acid etched) [3,21]. For example, smooth, press-fit acetabular cups for THR reportedly provided unsatisfactorily high failure rates even when HA-coated [22,24,25], whereas HA-coated threaded cups gave much better results [3,26].

The current trend in research and industrial practice is therefore to manufacture thin ($\leq$50 μm) HA layers, which do not alter the abovementioned textural features [28–30]. Additionally, thinner coatings usually contain less residual stress, reducing the risks of delamination [31,32]. Such low thicknesses are barely attainable by plasma-spraying, since the deposition of a homogeneous dense (the porosity of commercially available coatings is usually $\leq$10% [3,6,11,22,33–35]) ceramic

* Corresponding author. Tel.: +39 0592056233; fax: +39 0592056243.
E-mail address: giovanni.bolelli@unimore.it (G. Bolelli).

layer by such technique requires the superposition of a sufficiently large number of lamellae. This implies a minimum limit for coating thickness, particularly because the need to retain some unmelted crystalline HA in the sprayed particles reduces their degree of flattening on the substrate [36]. Consequently, an electrodeposition technique has been explored in some publications [28–30] in order to reduce HA thickness to below 50 μm. Even more literature exists on the use of sol–gel methods for the deposition of thin hydroxyapatite films [37–45]. These methods are highly versatile; for instance, they allow the deposition of nanocomposite hydroxyapatite films reinforced with nanotubes [39], or of doped films containing elements such as F and Sr, in order to tailor the interaction with osteoblastic cells [40,41], or Ag, in order to provide an antibacterial action [42]. They also feature high productivity and relative ease of implementation [37,38].

Despite these advantages, the use of the sol–gel method on an industrial scale imposes a complete technological change, relative to state-of-the-art thermal spray processes. It also requires accurate control of the stability of the sols and of all the stages of coating formation, which include sol application, drying/gelation, and final conversion to crystalline hydroxyapatite [37–45]. When producing pure hydroxyapatite films (with no organic or polymeric additives), conversion is achieved by heat treatment of the coated component at temperatures which may be as high as 600 °C [40,42,43,45], 700 °C [43], 750 °C [44], 800 °C [45], 900 °C [37], or 1000 °C [41], for durations ranging from 5 to 15 min [45] up to 1 or more hours [40–44]. Such process can cause distortions and/or phase alterations in the substrate materials. Moreover, even though literature reports high adhesion strength of sol–gel hydroxyapatite to metal substrates [38,43], the heat treatment may induce thermal stresses in the coating. It has even been proposed to modify the substrate alloy composition in order to match its thermal expansion coefficient to that of the hydroxyapatite layer, to avoid this problem [45].

The present study therefore aims to implement an innovative thermal spray deposition technique, namely the High Velocity Suspension Flame Spraying (HVSFS) process, in order to deposit thin (≤50 μm), homogeneous hydroxyapatite layers on titanium plates. The HVSFS process overcomes the abovementioned limits of conventional plasma-spraying whilst retaining the basic advantages of all thermal spraying processes in terms of versatility and high productivity [46–53]. Most importantly, it avoids the need for extended heat treatments on entire coated parts, it does not involve major technology changes, and it does not require careful control over the stability of sols, provided that a stable suspension can be commercially procured.

This paper specifically investigates the microstructure, phase composition, and micromechanical properties of HVSFS-deposited HA coatings as a function of the process parameters and of the presence or absence of a ceramic bond coat (plasma sprayed TiO_2) between the HA layer and the titanium substrate. The possibility of controlling the crystalline phase content of coatings is also addressed.

The reactivity of the layers was tested by soaking in a simulated body fluid solution and their potential use as osteoconductive layers was evaluated by *in vitro* cell culturing tests (cytotoxicity and cytocompatibility tests).

2. Experimental

2.1. Preparation and characterisation of powders and suspensions

The hydroxyapatite (HA) suspension, provided by Ce.Ri.Col. S.p.A. (Sovigliana, Italy), consisted of diethylene glycol (DEG) containing 13 wt.% dispersed nanosized particles.

The morphology of the powder particles was characterised by TEM (JEM 2010, JEOL, Tokyo, Japan) and their size distribution was measured by laser scattering (Mastersizer 2000 with Hydro-2000S wet dispersion system, Malvern Instruments, Malvern, UK). The phase composition was investigated by X-ray diffraction (XRD: X'Pert PRO, PANAlytical, Almelo, The Netherlands) using Cu-Kα radiation from an emission tube operated at 40 kV, 40 mA.

Table 1
HVSFS deposition parameters and maximum substrate surface temperature measured during spraying.

Set n.	Propane flow rate (SL/min)	O_2 flow rate (SL/min)	Stand-off distance (mm)	Suspension feed rate (g/min)	Max. deposition T (°C)
#1	55	350	120	105.0	454
#2	45	300	120		414
#3	45	350	100		427
#4	55	300	100		550
#5	50	325	110		460

2.2. Coating of samples

The substrates, 50 mm × 50 mm × 3 mm plates of grade 2 titanium, were grit-blasted with corundum particles (260 μm average size) using a manual gun operating at a pressure of 6 bar, obtaining a roughness of Ra ≈ 3.3 μm, Rz ≈ 26.2 μm. Half of the plates were also coated with a ≈70 μm-thick atmospheric plasma-sprayed (APS) TiO_2 layer (bond coat), deposited using the same process parameters as in [51]. Its surface roughness, measured by stylus profilometry (Mahr Perthometer, Göttingen, Germany), was Ra ≈ 4.7 μm and Rz ≈ 34.5 μm.

The HA layers were deposited onto grit-blasted and bond-coated plates using the HVSFS technique, as described in detail in [46,50]. Briefly, the suspension was mechanically fed through an axial conical injector, with an exit orifice of 0.9 mm diameter, into a custom-made cylindrical-conical combustion chamber [49,54] of a Top Gun-G HVOF torch (GTV GmbH, Luckenbach, Germany).

The gun, mounted on a 6-axis robot (Stäubli, Bayreuth, Germany), was horizontally scanned in front of the stationary substrates, with a pass velocity of 600 mm/s and a vertical distance of 2 mm between consecutive passes (interpass spacing), corresponding to a ≈50% overlap between the stream footprints. Only one scanning cycle was performed. The substrates (both bare and bond-coated) were preliminarily preheated to ≈250 °C in two torch scanning cycles with no suspension injection. The surface temperature of the substrates was continuously monitored during the process using an infrared pyrometer (Keller HCW, Ibbenbüren-Laggenbeck, Germany).

Five distinct sets of process parameters were employed, as listed in Table 1.

An estimate of deposition efficiency, defined as the ratio between the mass of material deposited onto the substrate and the overall mass of solid material sprayed during the HVSFS process, was obtained by weighing the substrates before and after the deposition using an analytical scale (accuracy 0.01 g). Deposition efficiencies were in the range of 45–55%, but the weighing method was not accurate enough to identify differences between the deposition efficiencies produced by the 5 different sets of process parameters.

As a term of comparison for the structural, microstructural, and micromechanical characterisation, a HA layer was also deposited onto grit-blasted Ti plates by APS using a GTV F6 torch equipped with

Table 2
APS deposition parameters for the reference HA coating.

Feedstock powder: size distribution/manufacturer	22–45 μm/Ceram
Arc current (A)	500
Primary gas (Ar) flow rate (SL/min)	50
Secondary gas (H_2) flow rate (SL/min)	0
Arc voltage (V)	23
Stand-off distance (mm)	100
Gun traverse speed (mm/min)	300
Pass spacing (mm)	3
n. of cycles	6
Powder feed rate (g/min)	11

standard 6 mm-diameter nozzle. The process conditions, listed in Table 2, were selected in order to obtain >50% crystalline hydroxyapatite content, which is representative of the properties of the APS HA layers currently employed in prosthetic applications as reported for example in [3,6,11,12,19,22,28,29,33,55–58].

2.3. Structural and microstructural characterisation of the coatings

Cross-sections of the HVSFS and APS HA layers were prepared by cold-mounting in polyester resin, grinding with SiC papers (up to 2500 mesh), and polishing with diamond slurries (up to 3 μm size) and colloidal silica suspension. They were then characterised by scanning electron microscopy (SEM: XL30, FEI, Eindhoven, The Netherlands) with energy dispersive X-ray (EDX) microanalysis (INCA: Oxford Instruments Analytical, Abingdon, UK). The thickness of the coatings was measured by image analysis (software: ImageJ version 1.43u, NIH, Bethesda, MD, USA) on SEM micrographs. Additional SEM + EDX analyses were made on fractured sections, obtained by breaking thin coated bars (cut from coated plates) in liquid nitrogen.

Fragments scraped from some of the HA coatings were employed for TEM imaging, for simultaneous differential thermal analysis + thermogravimetry (DTA + TG) tests, carried out in flowing air at a heating rate of 20 °C/min up to 1400 °C (STA 429: Netzsch, Selb, Germany), and for Z-potential assessments (Zetasizer Nano ZS, Malvern Instruments). Z-potential was obtained from measurements of electrophoretic mobility (U_E) through the Henry equation in Smoluchowski approximation: $U_E = 2k\varepsilon Z / (3\eta)$, where ε = dielectric constant; η = viscosity; Z = Z-potential; k = constant = 1.5. For these measurements, a suspension with 1 g/L solid content was obtained by dispersing the scraped powder in distilled water; the pH was adjusted by mixing the suspension with commercially available saline buffer solutions (Sigma-Aldrich Fluka) in a volume ratio of 3:1. The actual pH value of the buffered suspension was determined immediately before the Z-potential measurement. As a term of comparison, the same Z-potential measurements were carried out on the pure crystalline hydroxyapatite powder used as feedstock for the APS depositions (Table 2).

The structural features of the coatings were assessed by XRD on top surfaces and by micro-Raman spectroscopy (LabRam: Horiba Jobin-Yvon, Villeneuve D'Ascq, France), performed on polished cross-sections using a 632.81 nm-wavelength He–Ne laser source focused through a 100× lens.

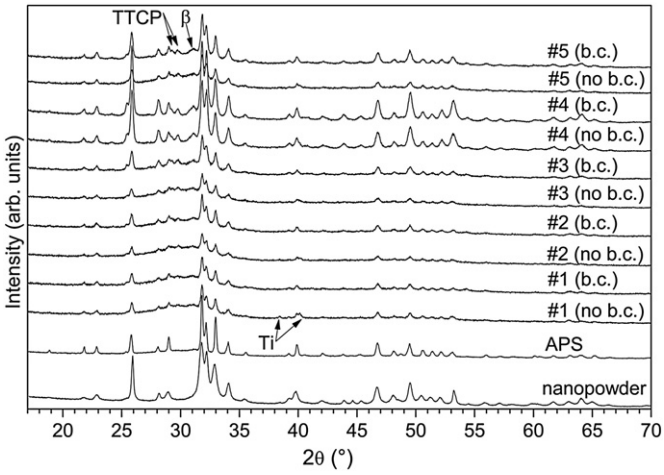

Fig. 2. XRD patterns of the HA nanopowder, of the HVSFS-deposited coatings, and of the APS reference. Legend: TTCP = tetracalcium phosphate $4CaO{\cdot}P_2O_5$ (JCPDF 25-1137); β = β-tricalcium phosphate $Ca_3(PO_4)_2$ (JCPDF 9-169); Ti = titanium (JCPDF 44-1294); peaks not labelled = hydroxyapatite $Ca_{10}(PO_4)_6(OH)_2$ (JCPDF 9-432).

The amount of crystalline hydroxyapatite phase was quantified by acquiring the pattern of a pure microcrystalline HA powder (Captal 60, Plasma Biotal, Tideswell, UK) under identical operating conditions and by computing the integrated intensities of the (2 1 1), (1 1 2) and (3 0 0) diffraction peaks, nominally located at 2θ angles of 31.8°, 32.2°, and 32.9° respectively (according to the JCPDF 9-432 powder diffraction file), for both the coatings and the reference powder, in accordance with [59]. The ratio between the integrated intensities of the diffraction peaks of the coatings, and of the reference powder, provided the desired quantification.

The micro-Raman spectra were also fitted with Gaussian peak functions as shown in [60,61], when the peaks of crystalline hydroxyapatite were distinguishable from those of other crystalline and glassy phases: the amount of crystalline hydroxyapatite was defined as the ratio between the integrated area of the hydroxyapatite peak and the overall integral area of all peaks.

Further XRD patterns were acquired on low crystallinity samples after heat treating in air using an electric furnace, in order to investigate the re-crystallisation behaviour of HVSFS coatings. Treatment temperatures were selected based on DTA + TG results (see Section 3.1). In all

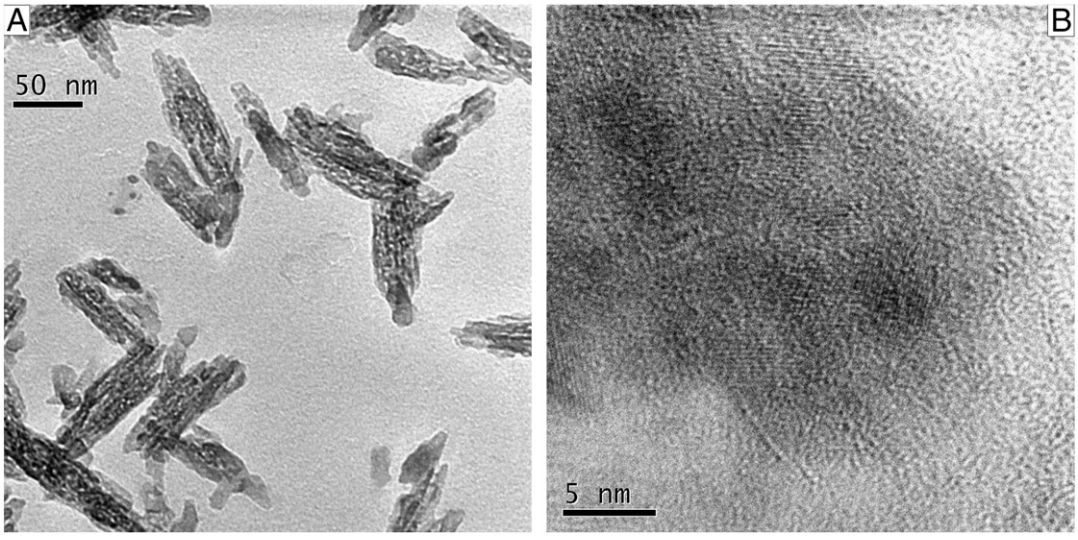

Fig. 1. TEM micrographs (A: overview; B: high resolution) of the hydroxyapatite powder.

cases, the heating rate was 10 °C/min and the isothermal treatment duration was 1 h. The samples were then slowly cooled inside the furnace.

2.4. Mechanical characterisation of the coatings

The hardness and elastic modulus of the HVSFS and APS HA coatings were assessed by depth-sensing Berkovich nano-indentation (NHT: CSM Instruments, Peseux, Switzerland). Forty indentations were performed on the centreline of the polished cross-section of each sample, with prescribed maximum penetration depth of 500 nm, loading and unloading rates of 70 mN/min, and holding time at maximum load of 15 s. The results were analysed according to the Oliver–Pharr method, as prescribed by the ISO 14577 standard, and the Poission's ratio of the material was assumed to be 0.23. The average ± standard deviation of hardness and

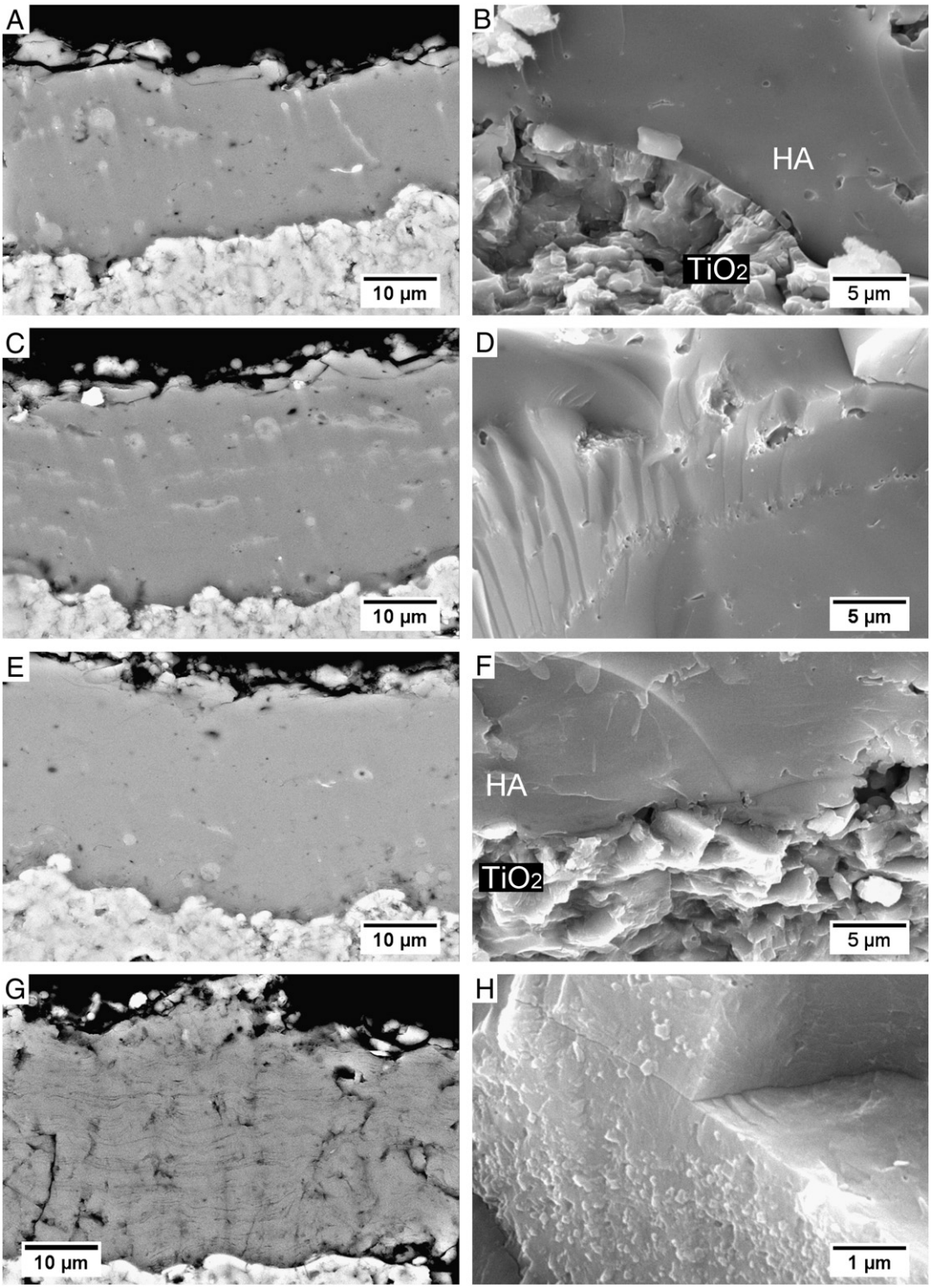

Fig. 3. SEM micrographs of HA samples #1 (A: polished section; B: fracture section), #2 (C: polished section; D: fracture section), #3 (E: polished section; F: fracture section), #4 (G: polished section; H: fracture section), #4 without bond coat (I: polished section; L: fracture section), #5 (M: polished section; N: fracture section), and of the APS reference (O). All samples deposited onto TiO_2 bond coat except where noted. In panels B, F, the HA/TiO_2 bond coat interface is also shown; in panel I, the dashed line indicates the boundary between two morphologically distinct layers; in panel O, the arrows indicate unmelted inclusions.

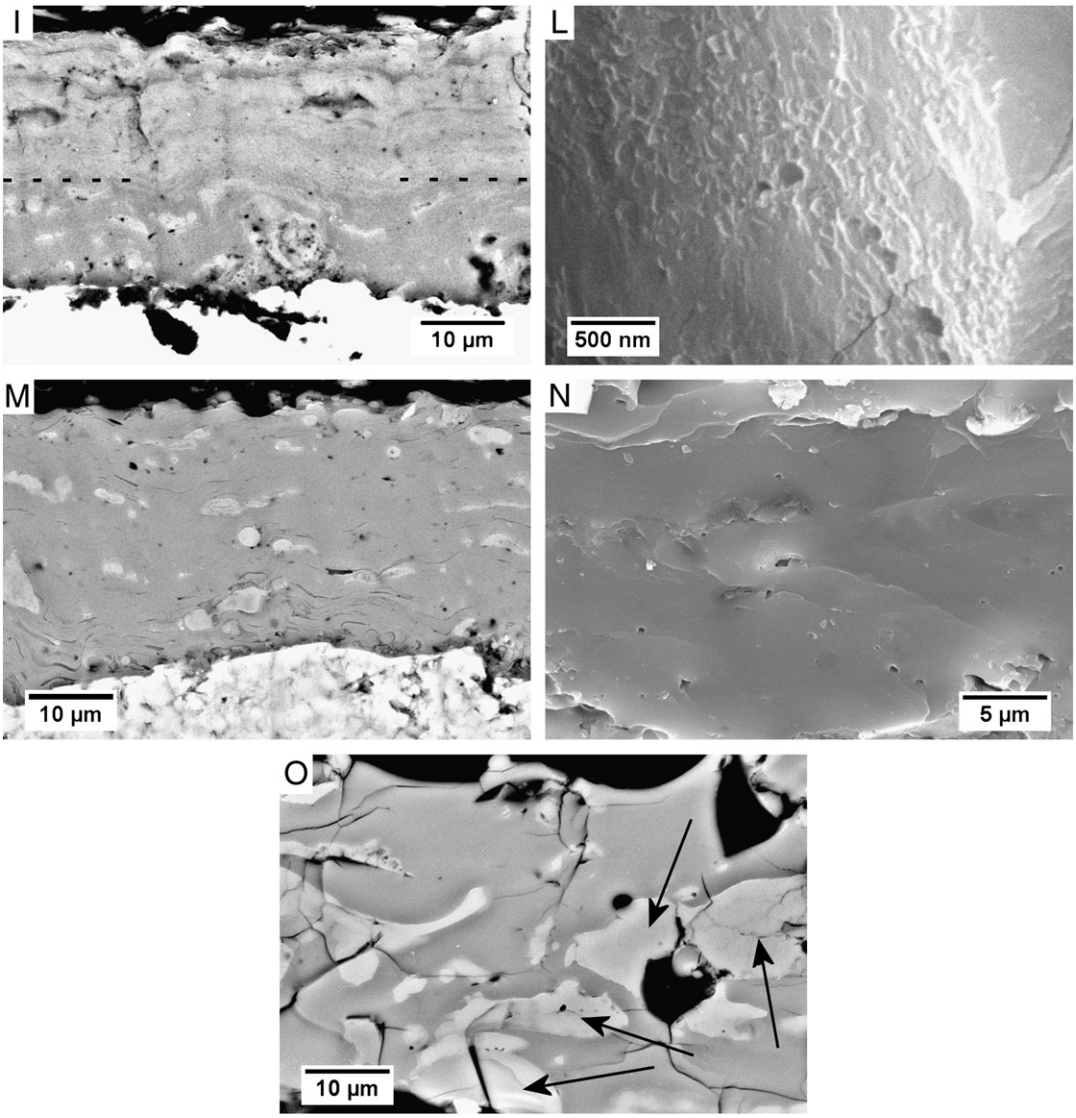

Fig. 3 (*continued*).

elastic modulus were assessed for each coating. The data were also fitted to the Weibull probability function $F(x) = 1 - e^{\left(\frac{x}{x_0}\right)^m}$ (with $F(x_i) = i / (n + 1)$ probability associated to the i-th data point of a series of n data points [62]) in order to obtain the Weibull modulus m.

The adhesion strength of the HVSFS-deposited HA coatings was measured by tensile adhesion testing according to ISO 4624, following the experimental procedure described in [63].

2.5. Soaking tests in simulated body fluid (SBF) solution

Samples of 10 mm × 10 mm were cut from the coated plates and vertically immersed in plastic containers filled with 20 mL of simulated body fluid (SBF) solution, prepared according to the formulation given by Kokubo and Takadama [64]. The containers were kept at 37 °C in an environmental chamber (MPM Instruments, Bernareggio, Italy) and the SBF solution was changed every three days, in order to simulate the dynamic conditions encountered in living organisms. The samples were immersed for periods of 1, 3, 7, 14 days.

After extraction, the samples were rinsed with distilled water and dried in air. Their structural and microstructural features were assessed by XRD, by environmental SEM (ESEM: Quanta 200, FEI) investigation under low vacuum conditions (water vapour atmosphere at a pressure of ≈1 mbar), and by micro-Raman spectroscopy, performed both on top surfaces and polished cross-sections of soaked samples (the latter prepared according to the procedure described in Section 2.3).

2.6. In vitro cell interaction

In vitro cytotoxicity and cytocompatibility tests were performed using a human osteosarcoma cell line Saos-2 (CRL 1427) model. Samples ($10 \times 10 \times 3$ mm^3) of HA were obtained by mechanical cutting and disinfected by soaking in 70% ethanol solution and then rinsed in sterile D.I. water.

The culture medium used for both cytotoxicity and cytocompatibility tests is McCoy's 5A modified medium with 15% Fetal Bovine Serum (FBS), 2% sodium pyruvate and 1% penicillin/streptomycin. For cytotoxicity tests HA samples were immersed in the medium for 2 and 7 days maintaining a surface/medium ratio of 3 cm^2 mL^{-1}. Culture medium was also aged for 2 and 7 days and used as internal control.

After 2 or 7 days of incubation, medium extracts were put into contact with Saos-2 cells (density = 10^4 cells cm^{-2}) on 96-well tissue culture plates (TCPs). Cells were cultured for 24 h and cell viability was investigated by Alamar Blue colorimetric assay at an excitation wavelength of 510 nm and emission wavelength of 590 nm. Measurements for each specimen were triplicated.

In cytocompatibility tests, 7 specimens were incubated for two days in complete medium and then seeded using a cell density of 1×10^4 cells cm^{-2}. After 24 h, 3, and 7 days of incubation, cell viability onto HA specimens was assessed using Alamar Blue colorimetric assay (5 specimens for each time point). In order to evaluate cell morphology at each time-point, samples were prepared following a standard dehydration procedure based on different ethanol concentrations and then observed by SEM.

3. Results and discussion

3.1. Structure and microstructure of the coatings

The HA powder consists of nanometric particles (as nominally expected) of elongated, somewhat acicular shape (Fig. 1A), approximately 50 nm wide and 100–150 nm long. The equivalent diameters measured by laser scattering on the DEG-based suspension are $d_{10} =$ 94 nm, $d_{50} = 134$ nm, $d_{90} = 160$ nm. These values match reasonably well with TEM observations, provided that the highly irregular shape of the particles deviates widely from the ideal spherical geometry assumed in the laser scattering technique. XRD patterns confirm the presence of pure hydroxyapatite phase in this powder (Fig. 2), and quantitative computations (according to Section 2.3) accordingly indicate 100% crystalline hydroxyapatite content. High resolution TEM micrographs suggest that the powder particles are polycrystalline, with nanometric crystals (Fig. 1B). Their size was assessed from the XRD pattern using the Scherrer formula [65], using the integral breadths of the (102), (201), (211), (112), (300), (202) peaks of hydroxyapatite, all located in the small 2θ range comprised between 28° and 34° (according to JCPDF 9-432). The pattern was fitted using pseudo-Voigt peak functions and a polynomial background. The results show that crystal grain sizes are around 25 nm.

The HVSFS-deposited coatings appear homogeneous and free of large-scale defects, apart from some transverse microcracks (Fig. 3A–N). Their dense microstructure, with little porosity, resembles that of the HVSFS-deposited tricalcium phosphate (TCP) coatings characterised in [53], whereas it differs substantially from the more inhomogeneous appearance of the APS reference, which contains several unmolten rounded inclusions (Fig. 3O). In the cross-sections and fracture surfaces of the HVSFS layers, splats are nearly unrecognisable (Fig. 3A–N): they can only be identified on the top surfaces (Fig. 4A). Their size is much smaller than that of plasma-sprayed splats (Fig. 4B), with diameters ranging from a few micrometres down to ≤500 nm.

The typical ratio between splat diameter and original droplet diameter (i.e. the splat flattening ratio) for many HVSFS-deposited ceramics is ≈2 [53,66]. In particular, this flattening ratio was measured in [53] for TCP splats of micrometric size, deposited by HVSFS using process parameters similar to the present ones. This value can be extended to the present HA splats, also on account of the similarity between the thermo-physical properties of TCP and HA [53]. The present HVSFS-deposited HA coatings are therefore inferred to be primarily built up from the flattening of molten droplets of ≈0.5–1.5 μm diameter. Clearly, such droplets do not come from individual molten nanoparticles, but from the melting of micron-sized agglomerates of nanoparticles.

In accordance with classical descriptions of suspension spraying processes [67,68], the stream of the feedstock suspension was fragmented into liquid drops as it came into contact with the exhaust gas flow, after injection into the combustion chamber of the HVSFS torch. As diethylene glycol was evaporated from the drops, the solid fraction was released, primarily in the form of agglomerates. Agglomerates of 0.5–1.5 μm diameter suggest an original drop size of some micrometres. This matches well with finite element simulations, predicting liquid drop sizes of ≤10 μm [54] and down to ≈1 μm [69] after fragmentation of a liquid stream axially injected into a supersonic combustion gas jet.

SEM micrographs suggest that the reason the lamellae are almost unrecognisable across the coating cross-sections and fracture surfaces is presumably a result of splat boundary sintering (the circled area of Fig. 4A shows partial sintering between two lamellae on the top surface).

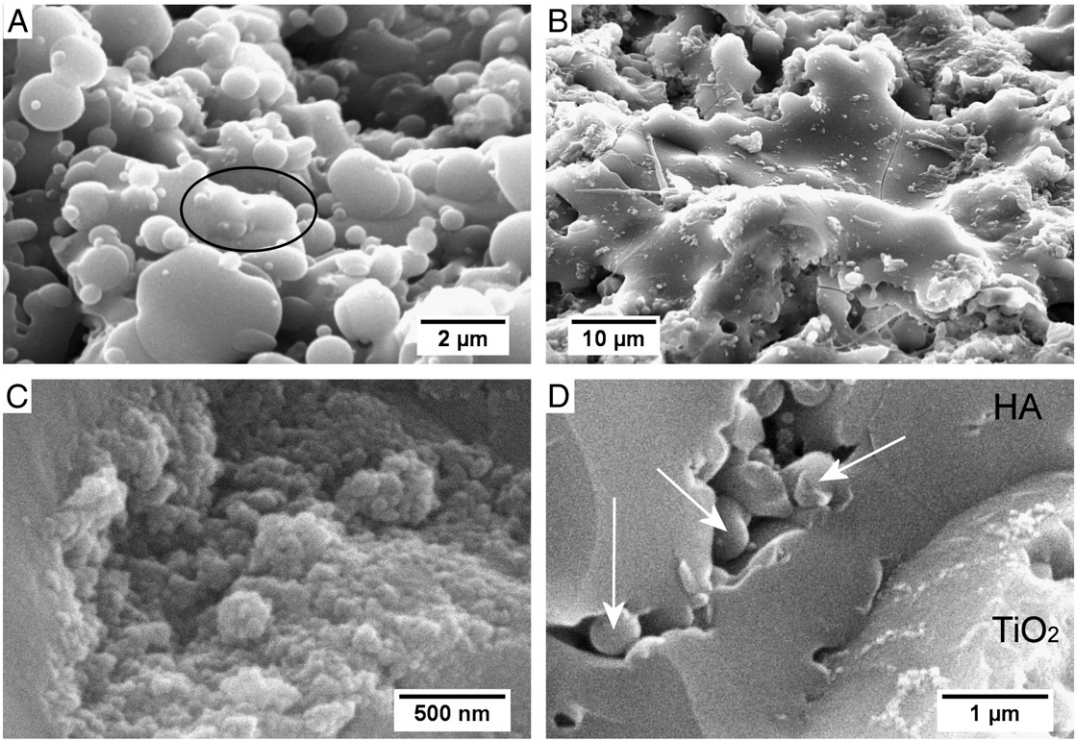

Fig. 4. Secondary electron SEM micrographs showing the surfaces of the HVSFS HA coating #1 (A) and of APS HA (B), viewed at an angle of 45°, and details (C, D) of the fracture surface (viewed at an angle of 35°) of the HVSFS HA coating #2 deposited onto the TiO_2 bond coat. In panel A, the circle indicates sintered splats; in panel D, the arrows indicate sub-micrometre-sized spherical particles inside small porosities.

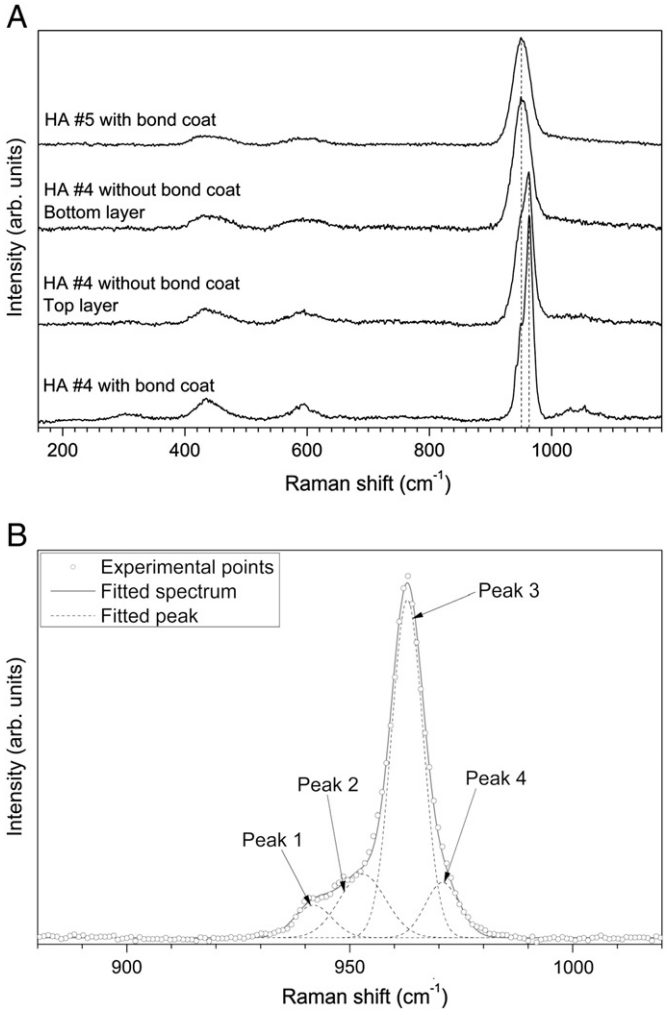

Fig. 5. (A) Micro-Raman spectra acquired on the cross-section of some HVSFS layers (the dashed lines indicate the exact position of the most intense peak) and (B) example of fitting of the 962 cm^{-1} peak in a spectrum acquired on HA sample #4 deposited onto the TiO_2 bond coat.

A significantly large number of fine particles impinge almost simultaneously onto the substrate during each pass of the torch. With an overlap of ≈50% between stream footprints during consecutive passes, approximately 13–19 μm thick layers are deposited during one cycle. Since splats are ≤500 nm thick (which is inferred from the previously estimated droplet diameters and from a flattening ratio of ≈2), at least 30–40 splats are deposited simultaneously on top of one another in molten condition, which allows for viscous flow sintering in spite of the high cooling rates, analogously to the mechanisms described in [53] for equally dense HVSFS TCP coatings.

Small, nanometric particles (Fig. 4C) or somewhat larger, micrometric or sub-micrometric rounded particles (Fig. 4D, arrows) are sometimes found inside the few porosities of these layers, corresponding to agglomerates which reached the substrate in unmelted or re-solidified conditions, respectively. The re-solidified agglomerates are very small in size, which presumably reflects the disruption of some original micron-sized aggregates into smaller ones and/or into individual nanoparticles, as proposed in [68] for a suspension plasma-spraying process. Due to their small size, they are easily cooled and deflected by the stagnation flow in front of the substrate. Many are lost, thus accounting for the deposition efficiencies no higher than 45%–55%, while the few which can stick to the surface are embedded in the coating in a re-solidified condition, as experimentally observed. This can be understood from a calculation of the Stokes number (St) of an individual nanoparticle. The Stokes number expresses the balance between the characteristic time scale of the aerodynamic response of a particle entrained in a turbulent viscous flow (τ_A) and the time scale of turbulent eddies in the viscous flow itself (τ_F) [70]:

$$St = \frac{\tau_A}{\tau_F} = \frac{\rho_P d_P^2 \Big/ 18\mu_G}{d \Big/ U}.$$

The turbulent feature under investigation is the stagnation flow, consisting of a gas layer flowing parallel to the substrate surface, approximately $d \approx 10$ mm thick [71]. A hydroxyapatite particle (density $\rho_P = 1356$ kg/m^3 [72]) with diameter $d_P = 134$ nm (i.e. the d_{50} equivalent diameter of the hydroxyapatite particles), entrained in a gas with dynamic viscosity $\mu_G \approx 65$ μPa·s (approximate viscosity of an exhaust gas mixture at 1600 °C [73]) flowing at a velocity U ≈ 800 m/s (velocity of the free HVSFS gas jet, 100–120 mm away from the torch nozzle exit [74]) is $St \approx 0.004$, i.e. much lower than unity. Individual nanoparticles therefore follow the stagnation flow along a trajectory parallel to the surface of the substrate plates [75]. Small agglomerates are less deflected, but their normal impingement velocity also decreases while they acquire a velocity component parallel to the substrate surface.

In greater detail, structural and microstructural differences are noted between the HA sample #4 with bond coat (Fig. 3G, H), the one without bond coat (Fig. 3I, L) and all the other HA samples (#1: Fig. 3A, B; #2: Fig. 3D, C; #3: Fig. 3E, F; #5: Fig. 3M, N).

The latter, irrespective of the presence or absence of the bond coat, exhibit smooth fracture surfaces (Fig. 3B, D, F, N), resembling that of bulk glass. These samples are found to consist mainly of a glassy phase, the presence of which is clearly revealed by XRD patterns, with the broad band occurring at 25° < 2θ < 35° (Fig. 2), and by the micro-Raman spectra (Fig. 5A). The main Raman peak, associated to the $\nu 1$ vibration mode of PO_4^{3-} tetrahedra, is very broad and located at 950 cm^{-1}, typical of glassy Ca phosphate [61,76]. The total amount of crystalline hydroxyapatite phase, assessed from the XRD patterns according to the procedure outlined in Section 2.3, never exceeds 24%, even though the TiO_2 bond coat seems to have a slight enhancement effect (Table 3). There are also small diffraction peaks of tetracalcium phosphate (TTCP: JCPDF 25-1137) and β-TCP (JCPDF 9-169) (Fig. 2).

In the XRD pattern of sample #4 sprayed onto the bond coat, the glassy band is much weaker, while the diffraction peaks of crystalline hydroxyapatite are stronger (Fig. 2), corresponding to an overall amount of 70% (Table 3). The sharper $\nu 1$ Raman peak located at 962 cm^{-1} also indicates crystalline hydroxyapatite as the main phase [77,78]. The Raman spectra of this sample can be fitted with Gaussian peak functions as described in Section 2.3 (Fig. 5B): four peak components were assumed, located at 942 cm^{-1} (β-TCP + TTCP: individual contributions are undistinguishable due to the overlap between their Raman peaks [60]), 953 cm^{-1} (glassy Ca phosphate), 963 cm^{-1} (hydroxyapatite), and 971 cm^{-1} (β-TCP [60]). The result, indicating 64% crystalline hydroxyapatite, is quite consistent with the XRD analysis. The rougher fracture surface (Fig. 3H) is accordingly characteristic of a polycrystalline material: consistently with such results, equiaxed, polygonal

Table 3
Thickness of the HVSFS-deposited HA coatings and of the APS reference (average ± standard deviation) from image analysis and content of crystalline hydroxyapatite phase from XRD pattern analysis.

Process parameter set	Thickness (μm)	Crystallinity (%) without bond coat	Crystallinity (%) with bond coat
#1	27 ± 3	14	14
#2	33 ± 5	8	14
#2	34 ± 2	11	22
#4	37 ± 4	47	70
#5	34 ± 4	16	24
APS reference	63 ± 12	62	N/A

nanocrystals were identified by TEM micrographs and by related SAED patterns (Fig. 6).

When sprayed onto bare grit-blasted Ti, by contrast, sample #4 exhibits a 2-layer structure, highlighted by dashed lines in Fig. 3I. The bottom layer, close to the substrate interface, is morphologically similar to samples #1, #2, #3, and #5 (Fig. 3I), and its micro-Raman spectrum indicates a mainly glassy structure (Fig. 5A). The top layer, by contrast, exhibits a rough fracture surface (shown in Fig. 3L), similar to that of sample #4 deposited onto the TiO_2 bond coat (compare to Fig. 3H). Its micro-Raman spectrum (Fig. 5A) accordingly reflects the presence of some crystalline hydroxyapatite, although the fitting procedure indicates a content of 41%, i.e. lower than that of the sample deposited onto the TiO_2 bond coat. XRD patterns also indicate a hydroxyapatite content of 47% (Table 3): this value mainly reflects the composition of the top layer, since the limited penetration depth of X-rays through HA results in most of the diffraction intensity being contributed by the top half of the coating (weak diffraction peaks of the substrate appear only in the diffraction pattern of the thinnest #1 sample, Fig. 2).

These peculiar structural and microstructural features can be explained as follows. In all of the HVSFS-deposited coatings, the cooling rate of the splats immediately after impact is very high ($\approx 10^7$ °C/s), and it decreases only when their temperature comes close to that of the substrate. This was shown, for instance, by numerical calculations on the previously mentioned HVSFS-deposited TCP splats [53].

At the incongruent melting point of hydroxyapatite (≈1570 °C [60]), the splats cool at such a high rate as to largely suppress the crystallisation process which would occur from the melt under thermodynamic equilibrium conditions (involving the nucleation and growth of TTCP and β-TCP from the phosphate melt and their subsequent peritectic reaction to yield hydroxyapatite). Due to the good glass forming ability of P_2O_5 [79], an undercooled melt is developed. Its formation is consistent with the previously noted occurrence of interlamellar sintering by viscous flow in all of the HVSFS-deposited samples: viscous flow is enabled by the formation of an undercooled melt, whereas it would be hindered or suppressed if direct crystallisation occurred at the very beginning of the cooling process.

As the undercooled melt approaches the average surface temperature of the coated system, its cooling rate decreases, and the development of a crystalline hydroxyapatite phase may become possible. However, during the deposition of HA samples #1, #2, #3, and #5, maximum surface temperatures of around or below 450 °C were attained (Table 1): in these cases, the splats did not remain at T > 450 °C for more than a few microseconds.

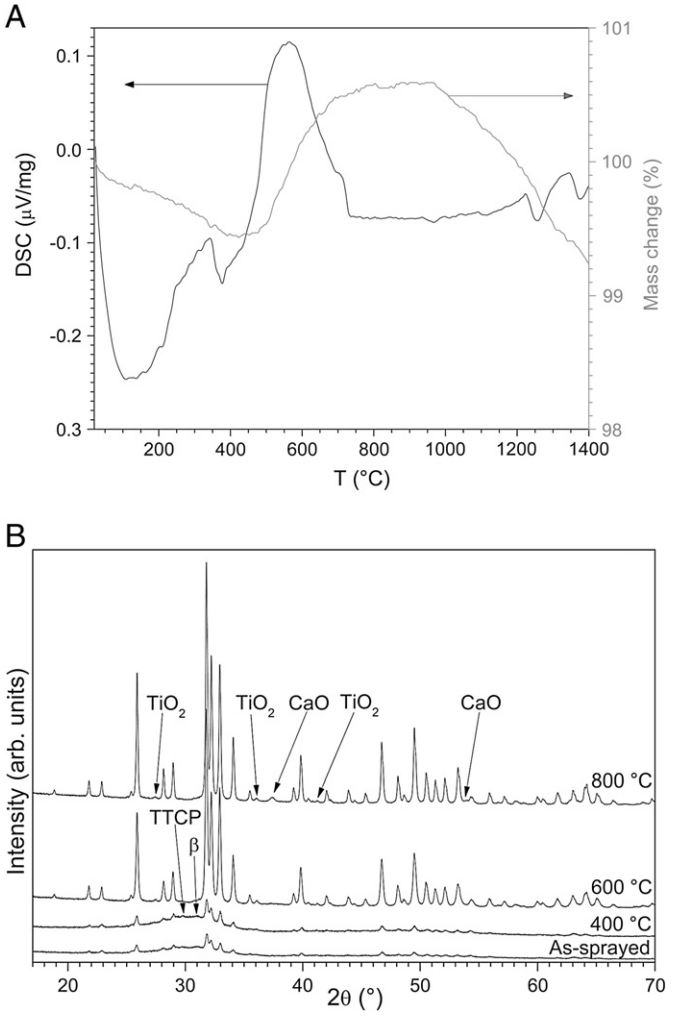

Fig. 7. DTA–TG curves acquired on powder scraped from HA sample #1 (A) and XRD patterns of HA sample #1 deposited onto the TiO_2 bond coat after heat treatment for 1 h in air at various temperatures (B). Legend of panel B: TTCP = tetracalcium phosphate $4CaO \cdot P_2O_5$ (JCPDF 25-1137); β = β-tricalcium phosphate $Ca_3(PO_4)_2$ (JCPDF 9-169); TiO_2 = rutile (JCPDF 21-1276); CaO = calcium oxide (JCPDF 37-1497), all unlabelled peaks = hydroxyapatite $Ca_{10}(PO_4)_6(OH)_2$ (JCPDF 9-432).

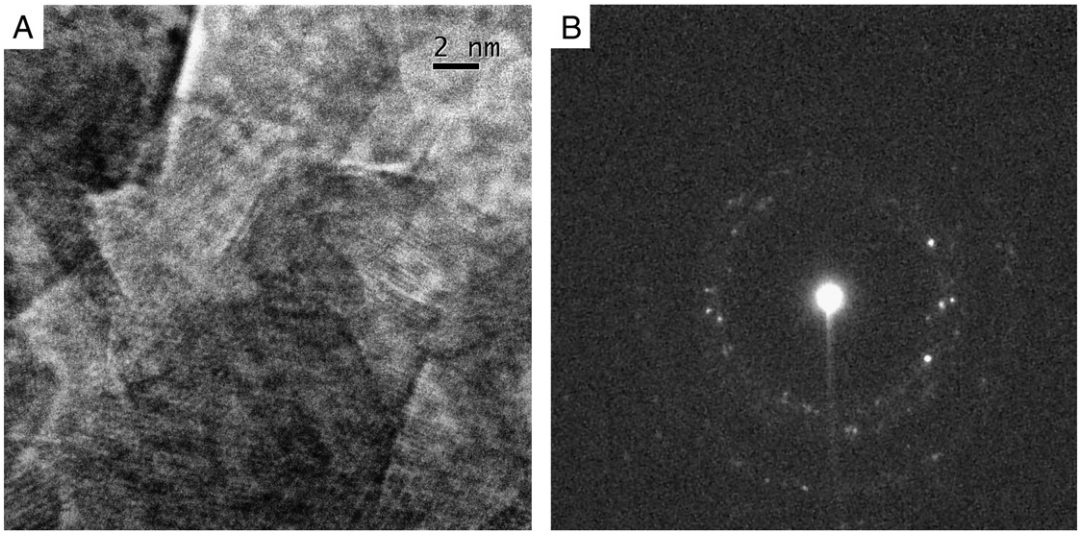

Fig. 6. TEM micrograph acquired on fragments scraped from HA sample #4 deposited onto the TiO_2 bond coat (A) and corresponding SAED pattern (B).

Table 4
Indentation hardness (H_{IT}) and elastic modulus (E_{IT}) obtained from nanoindentation testing of the HA coatings: average ± standard deviation, characteristic Weibull value (H_0; E_0) and Weibull modulus (m_H; m_E).

Sample	Indentation hardness H_{IT}			Elastic modulus E_{IT}		
	Average ± Std. dev. (GPa)	H_0 (GPa)	m_H	Average ± Std. dev. (GPa)	E_0 (GPa)	m_E
#1	2.9 ± 0.8	3.8	8.4	67 ± 12	75	9.7
#2	3.2 ± 0.5	3.4	6.9	66 ± 7	69	10.3
#3	3.7 ± 0.5	3.9	5.5	74 ± 9	77	8.9
#4 with bond coat	4.5 ± 0.4	4.6	5.4	94 ± 6	95	9.3
#4 w/o bond coat	Top layer: 4.2 ± 0.6	4.4	6.7	Top layer: 89 ± 4	92	12
	Bottom layer: 3.5 ± 0.6	3.7	5.0	Bottom layer: 84 ± 21	90	3
#5	3.7 ± 0.4	3.9	4.7	75 ± 10	82	9.1
APS	2.9 ± 0.6	3.1	3.3	56 ± 10	60	5.0

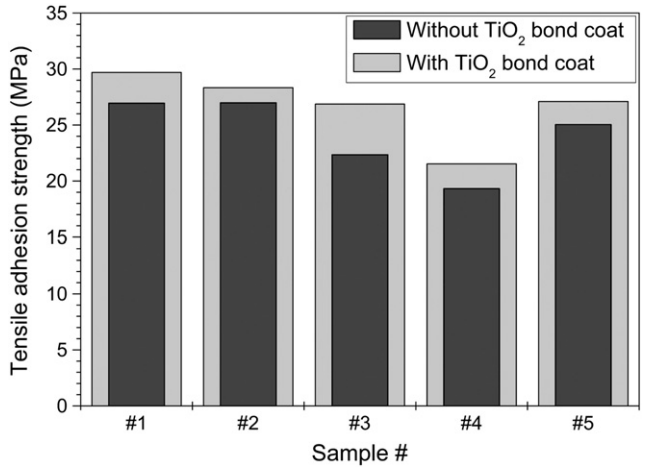

Fig. 8. Tensile adhesion strength of the HVSFS-deposited HA coatings.

In these conditions, re-crystallisation of hydroxyapatite is barely possible, since this process can only occur above 450 °C, as shown by DTA–TG measurements (Fig. 7A) and by XRD analysis on heat treated samples (Fig. 7B). DTA curves exhibit a broad exothermal peak ranging approximately from 450 °C up to 750 °C. This peak reflects the crystallisation of hydroxyapatite from glassy Ca phosphate, with an associated mass gain of 1.2% due to hydroxylation. After heat treatment performed at 400 °C (i.e. below the onset temperature of the DTA peak), no quantitative phase change occurs (Fig. 7B), whereas the content of crystalline hydroxyapatite in the samples (assessed as described in Section 2.3) rises to 85%–98% after heat treatments at 600 °C (around or immediately above the peak temperature, see Fig. 7A) and 800 °C (above the peak temperature). These results are consistent with previous thermal analyses of glassy Ca phosphate [80]. Interestingly, some CaO appears after treatment at 800 °C but not after treatment at 600 °C (Fig. 6B), which is perfectly consistent with [81], which states that CaO crystallises from glassy Ca phosphate together with hydroxyapatite starting from 698 °C. The slight weight loss at low temperatures in Fig. 7A is instead associated with the desorption of water molecules or of other adsorbed species from the surface of the scraped coating fragments, in accordance with [82,83].

HA samples #1, #2, #3, and #5 can therefore only contain a little crystalline hydroxyapatite, which may be partly contributed by a very limited extent of re-crystallisation in the splats, and partly by the embedment of a few unmelted agglomerates, as seen in Fig. 4B. The TTCP and β-TCP phases may derive from re-solidified agglomerates that experienced slightly lower cooling rates and may have had time to nucleate and grow crystalline phases at the incongruent melting point.

In contrast, when depositing sample #4 onto the TiO_2 bond coat, the maximum surface temperature of 550 °C (Table 1) exceeded the threshold for the onset of hydroxyapatite re-crystallisation (Fig. 7A), so that the undercooled melt in the flattened splats had considerably longer times (some seconds, corresponding to the time the system remains at the maximum surface temperature immediately after a torch pass) to re-crystallise. The equiaxed, nanocrystalline texture of this sample is indeed perfectly consistent with re-crystallisation of a largely undercooled melt, a process where homogeneous nucleation often prevails over heterogeneous nucleation and where the nucleation rate is usually high compared to the grain growth rate. If instead direct crystallisation had occurred as soon as the splat attained solidification temperature, columnar grains would have been developed by heterogeneous nucleation at the bottom of the splats, as normally occurs in conventional thermal spraying.

The high average surface temperature during deposition, which is the key to the marked crystallinity of this sample, can be ascribed, on one hand, to the greater heat delivered by the HVSFS gas jet to the substrate surface using parameter set #4, which features a low stand-off distance and an oxygen/fuel ratio close to unity (Table 1), implying the highest

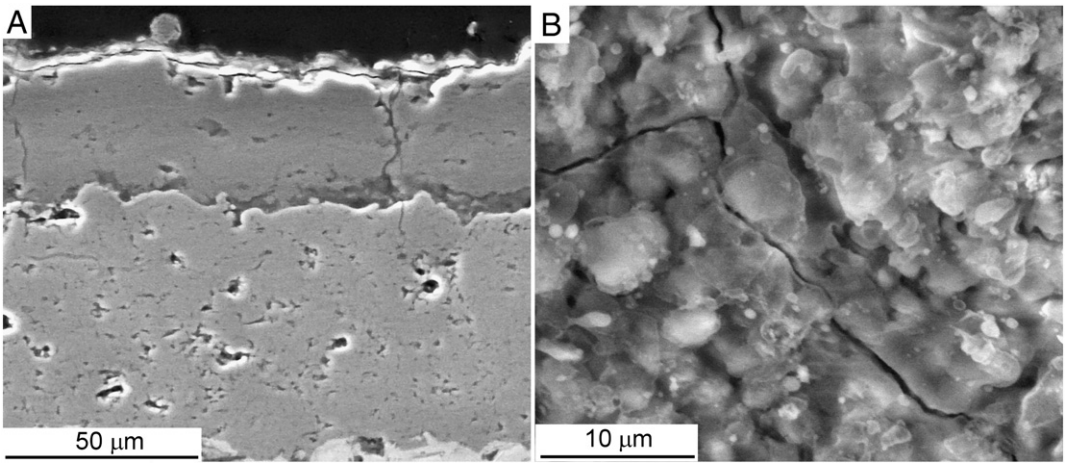

Fig. 9. SEM micrographs (secondary electrons) of the cross-section (A) and top surface (B) of HVSFS HA sample #4 deposited onto the TiO_2 bond coat, after 14 days of soaking in the SBF solution.

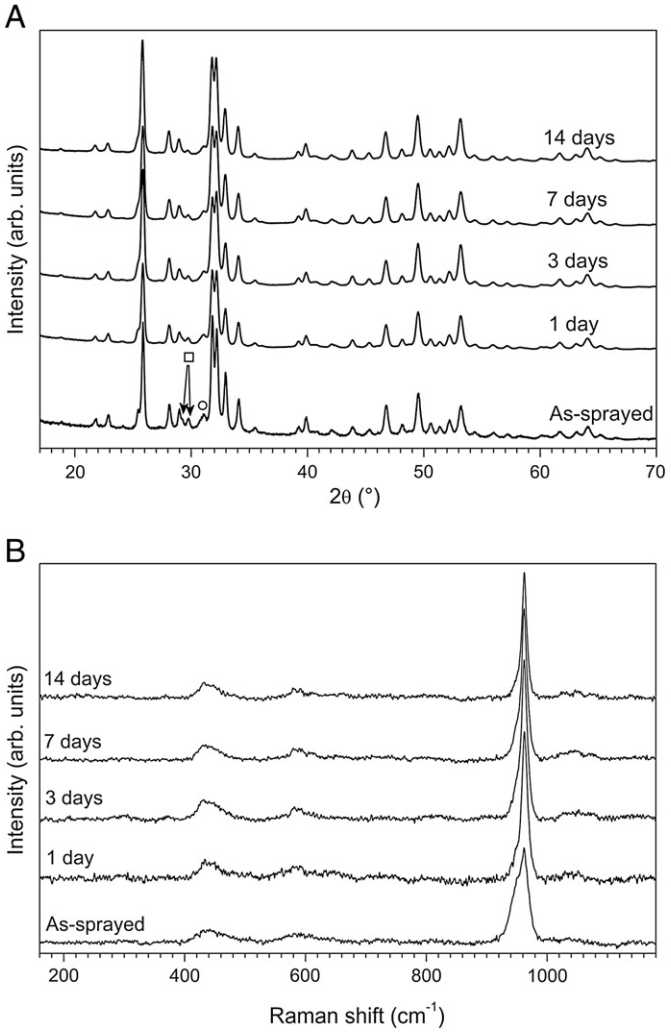

Fig. 10. XRD patterns (A) and Raman spectra (B) of HVSFS HA sample #4 deposited onto the TiO_2 bond coat, in as-deposited condition and after various soaking times in SBF. Legend of panel A: □ = tetracalcium phosphate $4CaO{\cdot}P_2O_5$ (JCPDF 25-1137); ○ = β-tricalcium phosphate $Ca_3(PO_4)_2$ (JCPDF 9-169); peaks not labelled = hydroxyapatite $Ca_{10}(PO_4)_6(OH)_2$ (JCPDF 9-432).

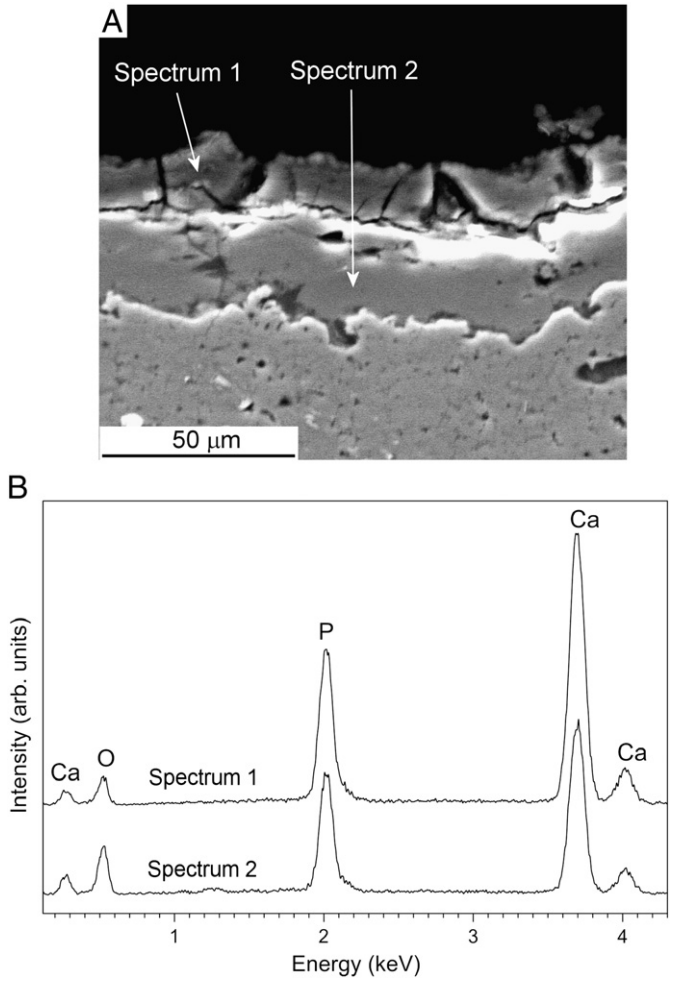

Fig. 11. Cross-sectional SEM micrograph (secondary electrons) of HVSFS HA sample #5 deposited onto the TiO_2 bond coat, after 3 days of soaking in SBF (A), and corresponding EDX spectra (B).

flame temperatures at the substrate location. On the other hand, the TiO_2 bond coat acted as a thermal insulating layer, slowing down heat extraction from the deposited material to the metal substrate. This favoured immediate attainment of the highest surface temperature during deposition and its persistence for a longer time. The thermal conductivity of bulk TiO_2 (8.5 W/(mK) at 20 °C and 3.9 W/(mK) at 400 °C [84]) is indeed intrinsically lower than that of Ti grade 2 (20.8 W/(mK) at 20 °C and 18.1 W/(mK) at 400 °C [84]), and, with an atmospheric plasma-sprayed TiO_2 layer, it is further reduced by the presence of pores, microcracks and interlamellar defects [85]. It is important to observe, however, that the TiO_2 bond coat starts to play a significant role only in combination with sufficiently "hot" process parameters.

In these conditions, the importance of the TiO_2 bond coat as a thermal insulator, as previously noted by Heimann et al. [36,60], is also clear from the fact that, when it is not employed, even with process parameter set #4, the higher thermal conductivity of the bare Ti substrate rapidly quenches the first layer of deposited material to below the 450 °C threshold, suppressing crystallisation. Because of the 50% overlap between stream footprints, during each pass of the torch, part of the material is not sprayed directly onto the substrate, but onto the ceramic layer deposited during the previous pass. The temperature of this layer is presumably still higher than the original pre-heating temperature of the substrate, and its thermal conductivity is lower than that of bare Ti. The surface temperature can, at this point, reach up to 550 °C using parameter set #4, and the new layer can re-crystallise, even though not as extensively as with the TiO_2 bond coat, presumably because heat extraction from the bare metal substrate is, in any case, faster and the maximum surface temperature is maintained for a shorter period.

When the new layer is deposited, the previous layer is also reheated, but this is clearly not sufficient to induce re-crystallisation. A similar phenomenon occurred in [49] during multi-cycle HVSFS deposition of HA coatings: in that case, a structural gradient was developed between different layers sprayed during consecutive cycles. It is inferred that a thermal gradient exists across the coating during spraying, so that the temperature in the bottom layer, close to the substrate interface, is not as high as that of newly deposited material on the outer surface.

It can therefore be postulated that, by controlling the process parameters and by the optional addition of a ceramic bond coat, an adjustable balance between quenching and re-crystallisation phenomena can be achieved in HVSFS-deposited layers, so that crystallinity can be varied across a wide range, while maintaining the same dense, homogeneous microstructure. Conversely, in plasma-sprayed HA layers an increase in the crystalline hydroxyapatite content requires the embedment of unmelted material, which compromises the density and homogeneity of the layer.

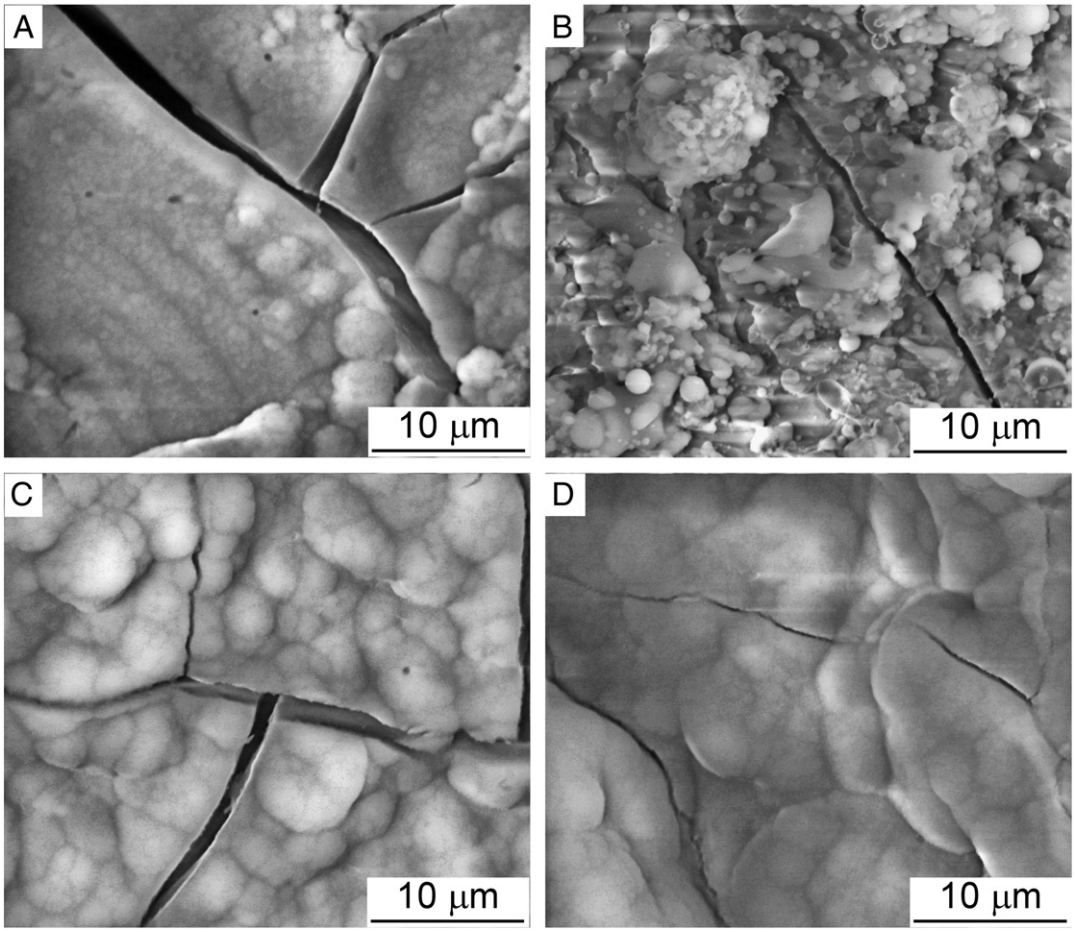

Fig. 12. SEM micrographs (secondary electrons) of the top surface of HVSFS HA sample #3 deposited onto the TiO_2 bond coat, after 1 day of soaking in SBF (A: area covered by precipitate layer; B: area not covered by precipitate layer), after 3 days (C), and after 7 days (D).

3.2. Micromechanical properties of coatings

All of the HVSFS-deposited HA layers with low crystallinity (samples #1, #2, #3, and #5) exhibit similar indentation hardness and elastic modulus (around 3.5 GPa and 70 GPa respectively, Table 4), irrespective of the presence or absence of the TiO_2 bond coat. As noted in Section 3.1, these layers are indeed all similarly dense and they all consist mainly of glassy Ca phosphate. The crystalline hydroxyapatite content does not vary enough to affect the mechanical properties in a perceivable way. Adhesion strength values are also relatively unaffected by process parameters (Fig. 8), but are enhanced by the TiO_2 bond coat. While the higher surface roughness (Section 2.2) and the different surface profile of the plasma-sprayed TiO_2 bond coat compared to the grit-blasted Ti substrate can enhance mechanical bonding, it is also true that the higher chemical affinity of hydroxyapatite with an oxide ceramic surface can also make an important contribution, as mentioned in [36,60]. The enhancement in adhesion strength is obtained in spite of the fact that the TiO_2 bond coat, whose thermal expansion coefficient is $\alpha \approx 7.5 \cdot 10^{-6}\ °C^{-1}$ [84], presumably worsens the thermal expansion mismatch between the Ti substrate ($\alpha \approx 8.6 \cdot 10^{-6}\ °C^{-1}$ [84]) and the HA coating ($\alpha \approx 13–17 \cdot 10^{-6}\ °C^{-1}$ [45,86,87]) as the system cools down after spraying.

Sample #4 deposited onto the TiO_2 bond coat is significantly harder and possesses greater elastic modulus (Table 4). Due to its larger crystallinity, its mechanical properties tend to approach those of bulk hydroxyapatite ($H \approx 6–7$ GPa [88–90], $E \approx 100–120$ GPa [89–91]), although they remain somewhat inferior, due to the residual presence of glassy phases, secondary crystalline phases (TTCP and β-TCP), and a few pores and microcracks (Section 3.1).

Its tensile adhesion strength, by contrast, is lower than that of samples #1, #2, #3, and #5 deposited both onto the bond coat and onto bare Ti (Fig. 8). This is probably due to the higher deposition temperature (Table 1), which is expected to induce higher tensile stresses after the system has cooled down to room temperature. It may also be due to the re-crystallisation of hydroxyapatite. The crystallisation of a glassy phase typically involves a decrease in specific volume, which is likely to contribute further tensile stresses. However, the adhesion strength of about 25 MPa is still comparable or superior to literature values for HA coatings deposited by conventional thermal spraying techniques [92–96] and far exceeds the minimum threshold of 15 MPa stipulated in the ISO 13779-2 standard.

When deposited onto bare Ti, the adhesion of sample #4 is further decreased, on account of the previously discussed favourable effect of the TiO_2 bond coat on adhesion. In this sample, instead of performing a single series of indentations along the centreline of the cross-section, two different sets of measurements were carried out along the centreline of each of the two layers identified in Section 3.1 and in Fig. 3M. Consistently with the respective structural features, the top layer, with higher crystallinity, possesses hardness and elastic modulus close to those of the corresponding sample deposited on the TiO_2 bond coat, whereas the glassy bottom layer has similar hardness to the glassy HA samples #1, #2, #3 and #5 (Table 4). The elastic modulus of the bottom layer could not be reliably evaluated by this nano-indentation technique, as the data was very widely scattered (see the high standard deviation in Table 4). This is probably due to the proximity of the substrate, in relation to the indentation size. The maximum penetration depth during indentation testing in the bottom layer was 0.5 μm and

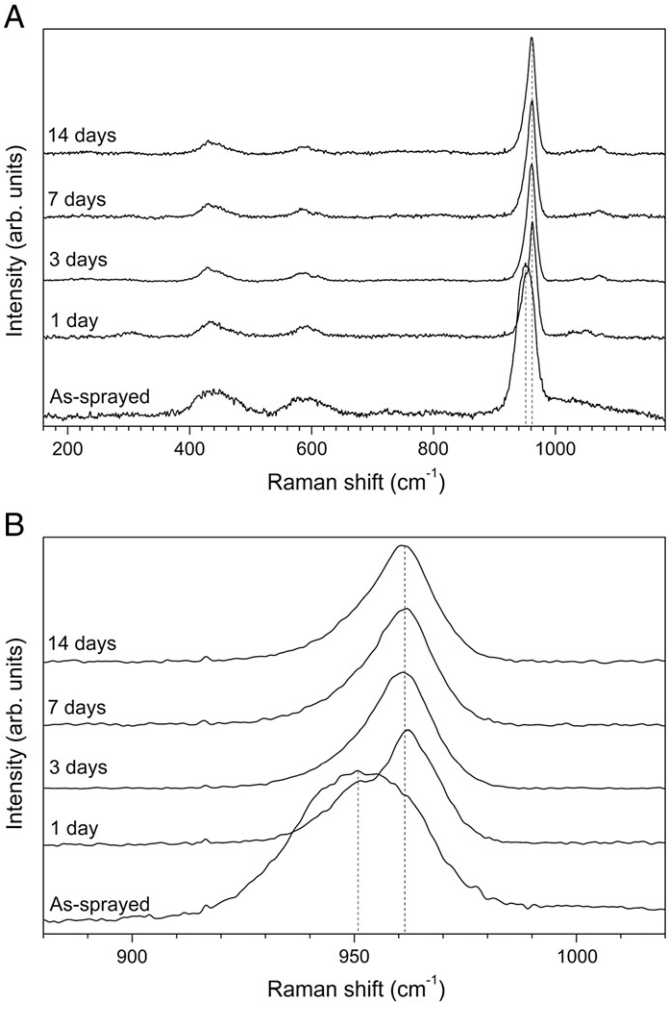

Fig. 13. Raman spectra of sample HVSFS HA #5 after soaking in the SBF solution for various times, compared to that of the as-deposited layer. A: overview; B: detail of the $\nu 1$ peak.

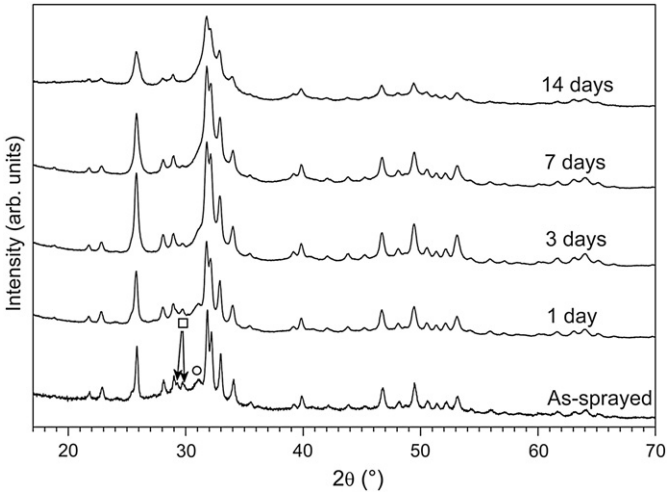

Fig. 14. X-ray diffraction patterns acquired on the top surface of the HVSFS HA sample #5 deposited onto the TiO_2 bond coat, in as-deposited condition and after soaking in the SBF solution for various times. Legend: □ = tetracalcium phosphate $4CaO{\cdot}P_2O_5$ (JCPDF 25-1137); ○ = β-tricalcium phosphate $Ca_3(PO_4)_2$ (JCPDF 9-169); peaks not labelled = hydroxyapatite $Ca_{10}(PO_4)_6(OH)_2$ (JCPDF 9-432).

so the lateral size of the indentation marks was about 3.5 μm. The distance between the indentation edges and the boundaries of the bottom layer (of thickness ≈ 13 μm and inferable from SEM micrographs, Fig. 3I) is therefore around 5 μm. In these conditions, the plastic deformation field produced by the indentation falls mostly within the bottom coating layer, but the elastic deformation field extends well beyond the plastically deformed area, affecting a larger volume which comprises the substrate as well. At least some of the indentations are therefore likely to cause perceivable elastic deformation in some portion of the substrate. The elastic response of the sample during unloading of the indenter was therefore altered by the contribution of the substrate, returning unreliable, scattered modulus values, while hardness was relatively unaffected as the plastic deformation region remained confined within the HA layer. These different scale effects for hardness and elastic modulus during depth-sensing indentation testing have been demonstrated for example in [97]. Reducing the maximum penetration depth of the indenter to avoid this effect would have resulted in the indentation test probing an excessively small volume of material, which would not have been representative of the overall properties of the HA layer.

It can therefore be concluded that the HVSFS process, through the possibility of tailoring the structural features of the coatings without impairing their microstructural integrity, also offers the possibility of adjusting their mechanical properties (hardness, elastic modulus) accordingly. Conversely, the retention of crystalline hydroxyapatite in an APS HA layer, requiring the embedment of unmelted material, impairs the coating density (Section 3.1), and, consequently, its hardness and elastic modulus. In fact, the values measured on the reference APS HA layer (Table 4), which are consistent with most literature reports on similar coatings [63,92,98–100], are lower than those of all of the HVSFS samples.

Compared to the HVSFS coatings, the inhomogeneity of the APS sample also increases data scattering, which is clearly seen in the Weibull modulus (m_H, Table 4) values. The m_H and m_E values characterising the distributions of hardness and elastic modulus data for the present APS layer, which are consistent with the typical m_H values associated with the mechanical strength of plasma-sprayed HA in literature [94,101–103], are significantly lower than the values for the HVSFS-deposited HA coatings (Table 4). The latter Weibull modulus values are usually $m_H \geq 5$ for hardness and $m_H \approx 8$–10 for elastic modulus (with the exception of the elastic modulus data of the bottom layer of sample #4 deposited onto bare Ti, which are not significant as explained previously) and are all similar, as all of the HVSFS samples exhibit comparable microstructural homogeneity. They are compatible with the Weibull modulus of dense HVOF-processed ceramics [104].

3.3. Soaking tests in simulated body fluid (SBF)

The HVSFS-deposited HA coatings with predominantly glassy structure (samples #1, #2, #3, #5, with and without bond coat) exhibit fast reactivity during the soaking tests in SBF, whereas those with higher crystallinity (sample #4 with and without bond coat) appear more stable, which is consistent with existing literature on the behaviour of hydroxyapatite coatings in physiological environments as a function of their crystallinity [58,60].

Specifically, HA sample #4 deposited onto the TiO_2 bond coat exhibits no appreciable transformations after 14 days of soaking in the SBF solution. No precipitated layer is seen in cross-sectional SEM micrographs (Fig. 9A), the fine as-deposited splats are still recognisable on the top surface after up to 14 days of soaking (Fig. 9B), and both its XRD pattern (Fig. 10A) and Raman spectra (Fig. 10B) remain unaltered.

The reason for the stability of this sample resides primarily in the high content of crystalline hydroxyapatite, in accordance with literature [58,60]. The dissolution rate of hydroxyapatite in simulated body fluids is much lower than that of other crystalline or glassy Ca phosphate phases [6].

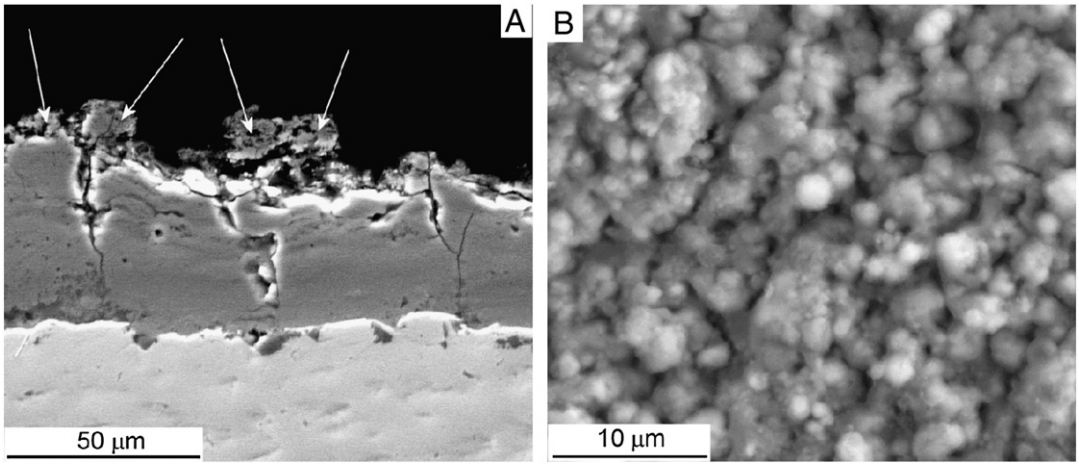

Fig. 15. SEM micrographs (secondary electrons) of the cross-section of sample HVSFS HA #4 deposited onto grit-blasted Ti, after 3 days of soaking in the SBF solution (A), and of the top surface of the same sample after 14 days of soaking (B).

However, in depth studies have revealed that, although crystalline hydroxyapatite does not dissolve readily in simulated body fluid solutions, it nevertheless tends to develop a precipitate bone-like hydroxyapatite layer on its surface [105]. The complex process described in [105] is triggered by the partial dissociation of hydroxyl (−OH) groups located on the surface of hydroxyapatite, leaving a negative surface charge. Ca^{2+} ions are attracted towards the negatively charged surface, forming an amorphous Ca-rich phosphate layer with positive surface charge. PO_4^{3-} groups then migrate to this positively charged surface, developing a negatively charged, Ca-deficient phosphate layer, which continues to grow and turns into a partly crystalline layer.

Since this process relies on the presence of hydroxyl groups, it becomes slower when hydroxyapatite has been de-hydroxylated by exposure to high temperatures. This is probably the case for the present coating. The thermal analyses discussed in Section 3.1 (Fig. 7A) accordingly showed that the glassy coatings are extensively de-hydroxylised, because of the high temperatures to which the feedstock particles are subjected in the HVSFS gas jet. Although the high peak surface temperature reached during the deposition of coating #4 was sufficient to trigger re-crystallisation of hydroxyapatite (Section 3.1), it is unlikely that complete re-hydroxylation could occur in the very brief time (a few milliseconds, Section 3.1) of the re-crystallisation process. The lack of hydroxyl groups in the coating therefore hinders the rapid development of the negative surface charge and delays all precipitation processes. Times longer than 2 weeks are probably needed in order to observe a perceivable formation of precipitate layers on the surface of coating #4 deposited onto the TiO_2 bond coat.

The behaviour of the glassy samples is completely different. Within three days, more than 1/3 of their original thickness is lost by dissolution into the SBF solution and replaced by a new, precipitated layer (Fig. 11A), which also consists of Ca, P, and O (Fig. 11B).

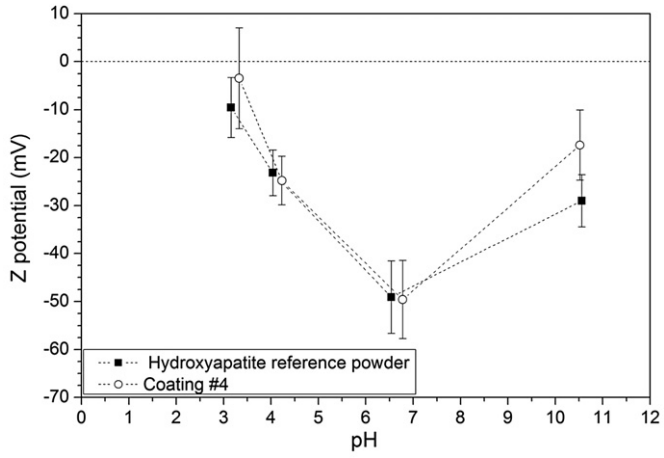

Fig. 16. Z-potential of a reference crystalline hydroxyapatite powder (full squares) and of powder scraped from sample #4 deposited without the bond coat (empty circles), plotted as a function of pH.

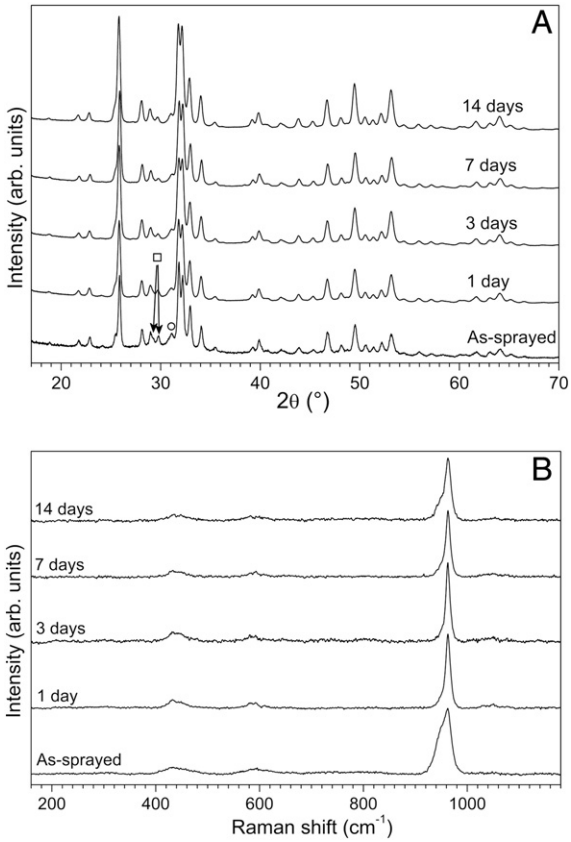

Fig. 17. XRD patterns (A) and Raman spectra (B) of HVSFS HA sample #4 deposited onto grit-blasted Ti, in as-deposited condition and after various soaking times in SBF. Legend of panel A: □ = tetracalcium phosphate $4CaO \cdot P_2O_5$ (JCPDF 25-1137); ○ = β-tricalcium phosphate $Ca_3(PO_4)_2$ (JCPDF 9-169); peaks not labelled = hydroxyapatite $Ca_{10}(PO_4)_6(OH)_2$ (JCPDF 9-432).

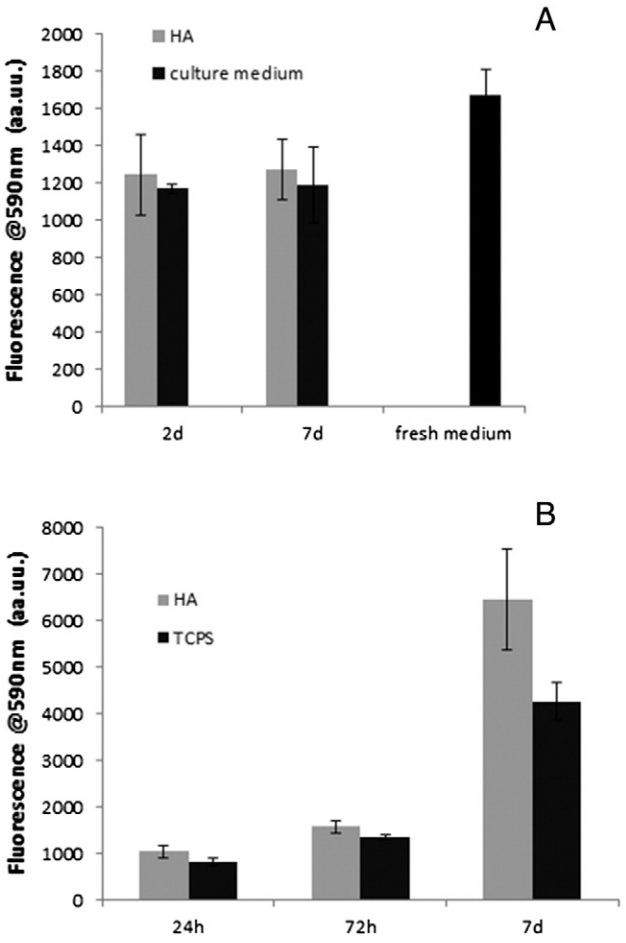

Fig. 18. *In vitro* viability Alamar Blue assays on Saos-2 cells: (A) cytotoxicity tests on fresh medium, aged medium, and HVSFS HA extract after 2 and 7 days; (B) direct cytocompatibility tests on HVSFS HA and TCPS.

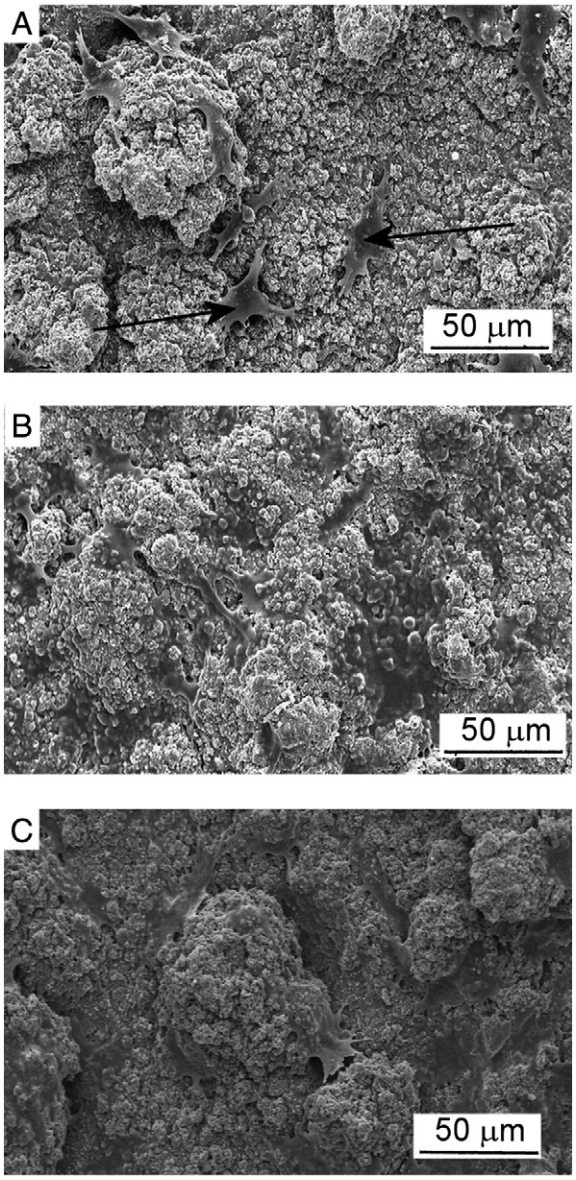

Fig. 19. SEM micrographs of Saos-2 cells on HVSFS HA coatings: (A) 1 day, (B) 3 days, and (C) 7 days. Arrows in panel A indicate some of the visible attached cells.

The precipitation starts early during the first day of immersion at some specific surface sites, where the typical spherulitic [105] or cauliflower-like surface morphology, usually found on this kind of layer [58,60,106], is developed (Fig. 12A). Other locations, by contrast, remain relatively unaffected after 1 day, with the original splats still quite clearly identifiable (Fig. 12B). In Raman spectra (Fig. 13A, B) the main $\nu 1$ peak of the as-deposited layers located at 950 cm^{-1} (see Section 3.1), transforms into a doublet with a main peak at 962 cm^{-1} and a shoulder at 950 cm^{-1}, indicating that the discontinuous precipitate layer consists of crystalline hydroxyapatite.

For increasingly long soaking times, complete coverage of the coating surface by the precipitate film occurs (Fig. 12C–D), in accordance with the cross-sectional micrographs (Fig. 11A). Raman spectra (Fig. 13A, B) transform into those of crystalline hydroxyapatite: the $\nu 1$ peak at 962 cm^{-1} now clearly prevails over the 950 cm^{-1} shoulder (Fig. 13B) and the $\nu 2$, $\nu 3$, and $\nu 4$ multiplets become more clearly defined.

XRD patterns confirm that the precipitate film consists of crystalline hydroxyapatite. It is observed that, as this layer progressively replaces the original coating for increasingly long soaking times, the glassy band and the diffraction peaks of secondary crystalline phases (TTCP and β-TCP) tend to disappear from the XRD patterns (Fig. 14), replaced by the diffraction peaks of hydroxyapatite. The significant breadth of these peaks implies that the crystalline lattice of the precipitated film contains significant lattice defects (such as partial substitution of carbonate ions in lattice positions), in accordance with literature [98,105–109].

The process of coating dissolution and its progressive replacement with a precipitate layer of poorly crystalline hydroxyapatite is consistent with available literature, which shows that glassy Ca phosphates readily dissolve in body fluids, releasing Ca^{2+} and PO_4^{3-} ions [58,60,106,107]. The mechanism differs from that described for pure crystalline hydroxyapatite by Kim et al. [105], since more extensive ion exchange occurs between glassy Ca phosphate and the physiological solution than is found with pure hydroxyapatite. The quick initial release of Ca^{2+}, reported by various authors [106,107], probably develops the necessary negative surface charge required to support the ongoing growth of the precipitate bone-like hydroxyapatite layer. Nucleation starts at some specific locations, as previously observed in [108], which may correspond to defects (e.g. pores, microcracks) of the original coating, where the exposed surface area is larger and the ion exchange mechanisms are consequently faster, or to areas where higher degrees of hydroxylation of the material was preserved [108].

An intermediate situation occurs with HA sample #4 deposited without bond coat, the top layer of which has higher crystalline hydroxyapatite content than that of samples #1, #2, #3, #5 but lower than that of sample #4 deposited onto the bond coat (Section 3.1). Its reaction with the SBF solution over the 14 day period is therefore slower

than that of the glassy samples, yet perceivable. A discontinuous precipitated layer appears from the third day of soaking (Fig. 15A, B), which turns into a uniform cauliflower-like layer after 14 days (Fig. 15C), although its morphology is not yet as developed as that of the more glassy samples (such as those shown in Fig. 12C, D).

The Z-potential of this sample, measured as a function of pH in diluted water-based buffer solutions, is similar to that measured for a pure hydroxyapatite powder (Fig. 16). The results obtained on the latter are consistent with the known Z-potential trends of crystalline hydroxyapatite: it attains a large negative Z-potential value of about −50 mV at pH ≈ 6.5 (similar to [110,111]) and approaches the isoelectric point at pH ≈ 3 (as reported in [112]). This confirms the validity of this powder as a reference sample. The negative Z-potential value of hydroxyapatite over a large pH range is generally ascribed to the dissociation of surface –OH groups, which releases H^+ ions into the solution leaving a negative surface charge (as mentioned in [105]), and to the PO_4^{3-} groups preferentially located on the surface of hydroxyapatite [110].

The similarity of the Z-potential trend of sample #4 deposited without the bond coat indicates that, in spite of some unavoidable thermal alteration, the spraying process did not modify substantially the surface chemistry of the material. The preserved negative surface charge is probably a key factor in triggering the precipitation of the hydroxyapatite layer seen in Fig. 15, according to the mechanisms outlined previously. The growth rate of this layer is indeed not matched by an equally fast dissolution of the coating itself, unlike the glassy samples (compare Fig. 15A to Fig. 12A). While some ion release is certainly occurring (unlike sample #4 deposited onto the bond coat), the observed negative surface must therefore be playing a pivotal role in favouring early nucleation and growth of the layer in this case.

The XRD pattern of this sample does not change over the testing period (Fig. 17A), since the thickness of this precipitated layer is too low to provide an appreciable contribution to the diffraction signal, while instead the Raman spectrum (Fig. 17B) exhibits a slight evolution. After 1 day of soaking, the main *v*1 vibration peak located at 962 cm^{-1} becomes somewhat sharper, which reflects partial dissolution of the glassy phase, the preliminary stage paving the way for the subsequent precipitation of the hydroxyapatite film as described above. After 3 and 7 days, most Raman spectra (such as the ones seen in Fig. 12D) do not change, as the precipitated layer is still discontinuous. The amount of Ca^{2+} and PO_4^{3-} ions released into the solution by the glassy phase is lower than in samples #1, #2, #3, and #5. After 14 days of soaking the layer becomes continuous, and so the Raman spectrum, reflecting the microcrystalline nature of this new layer, exhibits a slightly broader *v*1 peak, although its position does not shift, since no other phase apart from crystalline hydroxyapatite is contained within the precipitated layer.

It should be noted that, due to the crystallinity gradient of HA sample #4 sprayed onto bare Ti, faster dissolution of the underlying layer may be possible, if it comes into contact with the SBF solution. Although this was not seen in the present experiments (Fig. 15B), penetration of the SBF solution down to this layer may occur through the transverse microcracks existing in the HA coatings and may eventually lead to perceivable dissolution of the bottom layer for longer exposure times. This may undermine the adhesion of the more crystallised top layer with the substrate: in this respect, the structural gradient should probably be regarded as a potentially dangerous and undesirable feature.

3.4. In vitro indirect cytotoxicity and cell interaction

Cytotoxicity tests were performed on culture medium extracts in contact with HA HVSFS specimens for 2 and 7 days. Fluorescence values of Alamar Blue tests of Saos-2 cells cultured 24 h in culture medium extracts are summarized in Fig. 18A. Results are compared to fresh, 2-, and 7-day aged media. No significant differences ($P > 0.05$) were noticed between extracts, aged media (blanks), and fresh medium, indicating non-toxicity of the ions released by the HVSFS HA specimens.

Direct cell interaction tests were performed by direct culture of adhered Saos-2 cells. The morphology of cells in direct contact with HA HVSFS surfaces are shown in Fig. 19. After 24 h of incubation (Fig. 19A), cells had spread homogenously all over the HA surface (see arrows), extending their filopodia towards the surface asperities. By increasing the incubation time (Fig. 19B, C), cells spread all over the surface. SEM observations were confirmed by Alamar Blue assay, as summarized in Fig. 18B. An increase in fluorescence values was observed by increasing the culture time. Cells grew slowly in the first three days on both HA specimens and TCPS, while they grew faster from 72 h to seven days reaching over-confluence on TCPS after 7 days. At each time point, no significant difference was observed between cells cultured on HA samples and on TCPS (Fig. 18B), indicating no cytotoxic effects of HVSFS HA specimens on Saos-2 cells.

4. Conclusions

Hydroxyapatite (HA) coatings were deposited by HVSFS onto Ti grade 2 plates, either bare (grit-blasted) or preliminarily coated with a plasma-sprayed TiO_2 layer (bond coat), starting from a suspension of nanopowder feedstock.

The experimental characterisation activity led to the following conclusions.

- Dense, 27–37 μm thick HA layers were obtained, consisting of sintered splats originating from the impact and flattening of molten agglomerates of 0.5–1.5 μm in size. Hardness and elastic modulus of the HVSFS HA layers are higher than those of plasma-sprayed layers, and the scatter in mechanical properties is also lower (higher reliability). The adhesion strength of HVSFS HA coatings far exceeds the minimum requirements of ISO 13779-2.
- Direct crystallisation of hydroxyapatite is hindered in impact-quenched molten agglomerates. Re-crystallisation of hydroxyapatite from the resulting undercooled melt is possible if the average surface temperature of the system during HVSFS deposition is above the re-crystallisation threshold (≈450 °C), otherwise the undercooled melt turns into a glassy phase. The average surface temperature is controlled by process parameters and by the use of a thermally insulating TiO_2 bond coat limiting heat extraction to the metal substrate.
- The crystallinity of HVSFS-deposited HA coatings can therefore be adjusted from < 10% up to 70% without compromising the density and homogeneity of the coating, unlike conventional plasma-spraying.
- During immersion in the SBF solution, HA layers with low crystallinity are progressively dissolved and replaced by a new, precipitated hydroxyapatite layer, whereas highly crystalline layers are stable for up to 14 days of soaking.
  The negative surface charge of the hydroxyapatite material also has a role in favouring the nucleation and growth of the precipitated hydroxyapatite layer.
- SAOS-2 osteoblast-like cells adhered well and proliferated on HVSFS HA coatings with 47% crystalline hydroxyapatite on the outer surface. Cell viability was comparable to that on TCPS.

Further developments in this research will include a more detailed analysis of enzymatic parameters related to the responses of osteoblast-like cells cultured on these coatings, as well as experimental and numerical studies on protein adsorption. The latter phenomenon, which takes place during the earliest stages of implant contact with the body environment, is important in determining the preferential growth of bone tissues or of fibrous tissues onto the coated surfaces.

Acknowledgements

The authors are grateful to Ing. Susanna Borsari for her contribution to the experimental activities. Many thanks to Dr. Mauro Zapparoli (University of Modena and Reggio Emilia) for TEM micrographs, to Dr. Paola Miselli (University of Modena and Reggio Emilia) for DTA/TG analyses,

to Dr. Miriam Hanusková and Dr. Corrado Sciancalepore (University of Modena and Reggio Emilia) for guidance in the Z-potential measurements and to Dipl.-Ing. Andreas Vogel (University of Stuttgart) for the particle size distribution of the hydroxyapatite powder.

The Fondazione Cassa di Risparmio di Modena (project title: "Production, characterization and microstructural modeling of innovative coatings", Progetti di Ricerca a carattere internazionale) and the Vigoni Program (Project title: "Advanced thermally sprayed coatings for biomedical applications") are gratefully acknowledged.

References

[1] M.T. Manley, J.H. Dumbleton, K. Sutton, Fixation choices for primary hip and knee applications, Semin. Arthroplast. 17 (2006) 56–60.
[2] H.F. Morris, S. Ochi, Hydroxyapatite-coated implants: a case for their use, J. Oral Maxillofac. Surg. 56 (1998) 1303–1311.
[3] O. Reikerås, R.B. Gunderson, Long-term results of HA coated threaded versus HA coated hemispheric press fit cups: 287 hips followed for 11 to 16 years, Arch. Orthop. Trauma Surg. 126 (2006) 503–508.
[4] T. Albrektsson, C. Johansson, Osteoinduction, osteoconduction and osseointegration, Eur. Spine J. 10 (2001) S96–S101.
[5] R. Petit, The use of hydroxyapatite in orthopaedic surgery: a ten-year review, Eur. J. Orthop. Surg. Traumatol. 9 (1999) 71–74.
[6] L. Sun, C.C. Berndt, K.A. Gross, A. Kucuk, Material fundamentals and clinical performance of plasma-sprayed hydroxyapatite coatings: a review, J. Biomed. Mater. Res. 58 (5) (2001) 570–592.
[7] L. Visai, L. De Nardo, C. Punta, L. Melone, A. Cigada, M. Imbriani, C.R. Arciola, Titanium oxide antibacterial surfaces in biomedical devices, Int. J. Artif. Organs 34 (9) (2011) 929–946.
[8] L. De Nardo, L. Altomare, B. Del Curto, A. Cigada, L. Draghi, Electrochemical surface modifications of titanium and titanium alloys for biomedical applications, in: M. Driver (Ed.), Coatings for Biomedical Applications, Woodhead Publishing Ltd., Cambridge. UK, 2012, pp. 106–142.
[9] Y.-K. Lee, Y.-C. Ha, B.-K. Chang, K.-C. Kim, T.-y. Kim, K.-H. Koo, Cementless bipolar hemiarthroplasty using a hydroxyapatite-coated long stem for osteoporotic unstable intertrochanteric fractures, J. Arthroplast. 26 (4) (2011) 626–632.
[10] G.Y. Lee, A. Srivastava, D.D. D'Lima, P.A. Pulido, C.W. Colwell, Hydroxyapatite-coated femoral stem survivorship at 10 years, J. Arthroplast. 20 (7) (2005) 57–62.
[11] O. Reikerås, R.B. Gunderson, Excellent results with femoral revision surgery using an extensively hydroxyapatite-coated stem, Acta Orthop. 77 (1) (2006) 98–103.
[12] I. Landor, P. Vavrik, A. Sosna, D. Jahoda, H. Hahn, M. Daniel, Hydroxyapatite porous coating and the osteointegration of the total hip replacement, Arch. Orthop. Trauma Surg. 127 (2007) 81–89.
[13] W.N. Capello, J.A. D'Antonio, W.L. Jaffe, R.G. Geesink, M.T. Manley, J.R. Feinberg, Hydroxyapatite-coated femoral components. 15-year minimum followup, Clin. Orthop. Relat. Res. 453 (2006) 75–80.
[14] C.S. Ranawat, V.J. Rasquinha, M. Meftah, A.S. Ranawat, The hydroxyapatite-tapered stem: any added value? Semin. Arthroplast. 22 (2011) 75–78.
[15] P. Chandran, M. Azzabi, M. Andrews, J.G. Bradley, Periprosthetic bone remodeling after 12 years differs in cemented and uncemented hip arthroplasties, Clin. Orthop. Relat. Res. 470 (2012) 1431–1435.
[16] C. Courtney, B. Hooks, M.I. Froimson, Hydroxyapatite-coated, tapered titanium hip arthroplasty, Semin. Arthroplast. 20 (2009) 50–54.
[17] M. Degidi, A. Piattelli, P. Gehrke, P. Felice, F. Carinci, Five-year outcome of 111 immediate nonfunctional single restorations, J. Implantol. 32 (6) (2006) 277–285.
[18] I. Landor, P. Vavrik, A. Sosna, D. Jahoda, H. Hahn, M. Daniel, Hydroxyapatite porous coating and the osteointegration of the total hip replacement, Arch. Orthop. Trauma Surg. 127 (2007) 81–89.
[19] A. Paulsen, A.B. Pedersen, S.P. Johnsen, A. Riis, U. Lucht, S. Overgaard, Effect of hydroxyapatite coating on risk of revision after primary total hip arthroplasty in younger patients. Findings from the Danish Hip Arthroplasty Registry, Acta Orthop. 78 (5) (2007) 622–628.
[20] T. Uehara, K. Takaoka, K. Ito, Histological evidence of osseointegration in human retrieved fractured hydroxyapatite-coated screw- type implants: a case report, Clin. Oral Impl. Res. 15 (2004) 540–545.
[21] K. Rungcharassaeng, J.L. Lozada, J.Y.K. Kan, J.S. Kim, W.V. Campagni, C.A. Munoz, Peri-implant tissue response of immediately loaded, threaded, HA-coated implants: 1-year results, J. Prosthet. Dent. 87 (2002) 173–181.
[22] S.-Y. Kim, D.-H. Kim, Y.-G. Kim, C.-W. Oh, J.-C. Ihn, Early failure of hemispheric hydroxyapatite-coated acetabular cups, Clin. Orthop. Relat. Res. 446 (2006) 233–238.
[23] J.D. Voigt, M. Mosier, Hydroxyapatite (HA) coating appears to be of benefit for implant durability of tibial components in primary total knee arthroplasty. A systematic review of the literature and meta-analysis of 14 trials and 926 evaluable total knee arthroplasties, Acta Orthop. 82 (4) (2011) 448–459.
[24] J.-K. Chang, C.-H. Chen, K.-Y. Huang, G.-J. Wang, Eight-year results of hydroxyapatite-coated hip arthroplasty, J. Arthroplast. 21 (4) (2006) 541–546.
[25] K.-w. Cheung, S.-h. Yung, K.-ch. Wong, K.-h. Chiu, Early failure of smooth hydroxyapatite-coated press-fit acetabular cup — 7 years of follow-up, J. Arthroplast. 20 (5) (2005) 627–631.
[26] A. Tindall, K.D. James, R. Slack, Long-term follow-up of a hydroxyapatite ceramic-coated threaded cup. An analysis of survival and fixation at up to 15 years, J. Arthroplast. 22 (8) (2007) 1079–1082.
[27] J.-P. Vidalain, Twenty-year results of the cementless Corail stem, Int. Orthop. 35 (2011) 189–194.
[28] B.G. Bøe, S.M. Röhrl, T. Heier, F. Snorrason, L. Nordsletten, A prospective randomized study comparing electrochemically deposited hydroxyapatite and plasma-sprayed hydroxyapatite on titanium stems. 55 hips followed for 2 years with RSA and DXA, Acta Orthop. 82 (1) (2011) 13–19.
[29] M. Stilling, O. Rahbek, K. Søballe, Inferior survival of hydroxyapatite versus titanium-coated cups at 15 years, Clin. Orthop. Relat. Res. 467 (2009) 2872–2879.
[30] O. Reigstad, C. Johansson, V. Stenport, A. Wennerberg, A. Reigstad, M. Røkkum, Different patterns of bone fixation with hydroxyapatite and resorbable CaP coatings in the rabbit tibia at 6, 12, and 52 weeks, J. Biomed. Mater. Res. B Appl. Biomater. 99 (2011) 14–20.
[31] K. de Groot, J.G.C. Wolke, J.A. Jansen, Calcium phosphate coatings for medical implants, Proc. Inst. Mech. Eng. H J. Eng. Med. 212 (1998) 137–147.
[32] K.A. Gross, C.C. Berndt, Biomedical application of apatites, in: M.J. Kohn, J. Rakovan, J.M. Hughes (Eds.), Phosphates: Geochemical, Geobiological, and Materials Importance — Reviews in Mineralogy and Geochemistry, 48, 2008, pp. 631–672.
[33] M. Philippe, M. Ameil, Survival analysis at 10 years of a cohort of 297 atlas total hip prostheses, Eur. J. Orthop. Surg. Traumatol. 17 (2007) 573–578.
[34] Y.-Y. Chung, J. Kim, C.H. Lim, K.-S. Kim, Y.S. Lee, Measurement of extent of bone ongrowth and hydroxyapatite absorption in retrieved acetabular cups, J. Orthop. Sci. 13 (2008) 198–201.
[35] V. Borsari, M. Fini, G. Giavaresi, L. Rimondini, U. Consolo, L. Chiusoli, A. Salito, A. Volpert, R. Chiesa, R. Giardino, Osteointegration of titanium and hydroxyapatite rough surfaces in healthy and compromised cortical and trabecular bone: in vivo comparative study on young, aged, and estrogen-deficient sheep, J. Orthop. Res. 25 (2007) 1250–1260.
[36] R.B. Heimann, Thermal spraying of biomaterials, Surf. Coat. Technol. 201 (2006) 2012–2019.
[37] D. Alves Cardoso, J.A. Jansen, S.C.G. Leeuwenburgh, Synthesis and application of nanostructured calcium phosphate ceramics for bone regeneration, J. Biomed. Mater. Res. B Appl. Biomater. 100 (2012) 2316–2326.
[38] P. Choudhury, D.C. Agrawal, Sol–gel derived hydroxyapatite coatings on titanium substrates, Surf. Coat. Technol. 206 (2–3) (2011) 360–365.
[39] A. Abrishamchian, T. Hooshmand, M. Mohammadi, F. Najafi, Preparation and characterization of multi-walled carbon nanotube/hydroxyapatite nanocomposite film dip coated on Ti–6Al–4V by sol–gel method for biomedical applications: An in vitro study, Mater. Sci. Eng. C 33 (4) (2013) 2002–2010.
[40] P. Yin, F.F. Feng, T. Lei, X.H. Zhong, X.C. Jian, Osteoblastic cell response on biphasic fluorhydroxyapatite/strontium-substituted hydroxyapatite coatings, J. Biomed. Mater. Res. A (2013), http://dx.doi.org/10.1002/jbm.a.34723 (in press).
[41] C.J. Tredwin, G. Georgiou, H.-W. Kimc, J.C. Knowles, Hydroxyapatite, fluorhydroxyapatite and fluorapatite produced via the sol–gel method: bonding to titanium and scanning electron microscopy, Dent. Mater. 29 (5) (2013) 521–529.
[42] S. Samani, S.M. Hossainalipour, M. Tamizifar, H.R. Rezaie, In vitro antibacterial evaluation of sol–gel-derived Zn-, Ag-, and(Zn + Ag)-doped hydroxyapatite coatings against methicillin-resistant Staphylococcus aureus, J. Biomed. Mater. Res. A 101 (2013) 222–230.
[43] S. Zhang, Z. Xianting, W. Yongsheng, C. Kui, W. Wenjian, Adhesion strength of sol–gel derived fluoridated hydroxyapatite coatings, Surf. Coat. Technol. 200 (22–23) (2006) 6350–6354.
[44] A. Abdi Bastami, H. Farnoush, A. Sadeghi, J. Aghazadeh Mohandesi, Sol–gel derived nanohydroxyapatite film on friction stir processed Ti–6Al–4V substrate, Surf. Eng. 29 (3) (2013) 205–210.
[45] J. Breme, Y. Zhou, L. Groh, Development of a titanium alloy suitable for an optimized coating with hydroxyapatite, Biomaterials 16 (1995) 239–244.
[46] A. Killinger, M. Kuhn, R. Gadow, High-Velocity Suspension Flame Spraying (HVSFS), a new approach for spraying nanoparticles with hypersonic speed, Surf. Coat. Technol. 201 (2006) 1922–1929.
[47] G. Bolelli, V. Cannillo, R. Gadow, A. Killinger, L. Lusvarghi, J. Rauch, Properties of High Velocity Suspension Flame Sprayed (HVSFS) TiO_2 coatings, Surf. Coat. Technol. 203 (12) (2009) 1722–1732.
[48] G. Bolelli, J. Rauch, V. Cannillo, A. Killinger, L. Lusvarghi, R. Gadow, Microstructural and tribological investigation of High-Velocity Suspension Flame Sprayed (HVSFS) Al_2O_3 Coatings, J. Therm. Spray Technol. 18 (1) (2009) 35–49.
[49] N. Stiegler, D. Bellucci, G. Bolelli, V. Cannillo, R. Gadow, A. Killinger, L. Lusvarghi, A. Sola, High-Velocity Suspension Flame Sprayed (HVSFS) hydroxyapatite coatings for biomedical applications, J. Therm. Spray Technol. 21 (2) (2012) 275–287.
[50] G. Bolelli, V. Cannillo, R. Gadow, A. Killinger, L. Lusvarghi, J. Rauch, Microstructural and in vitro characterisation of high-velocity suspension flame sprayed (HVSFS) bioactive glass coatings, J. Eur. Ceram. Soc. 29 (2009) 2249–2257.
[51] D. Bellucci, G. Bolelli, V. Cannillo, R. Gadow, A. Killinger, L. Lusvarghi, A. Sola, N. Stiegler, High velocity suspension flame sprayed (HVSFS) potassium-based bioactive glass coatings with and without TiO_2 bond coat, Surf. Coat. Technol. 206 (2012) 3857–3868.
[52] L. Altomare, D. Bellucci, G. Bolelli, B. Bonferroni, V. Cannillo, L. De Nardo, R. Gadow, A. Killinger, L. Lusvarghi, A. Sola, N. Stiegler, Microstructure and in vitro behaviour of 45S5 bioglass coatings deposited by high velocity suspension flame spraying (HVSFS), J. Mater. Sci. Mater. Med. 22 (2011) 1303–1319.
[53] G. Bolelli, N. Stiegler, D. Bellucci, V. Cannillo, R. Gadow, A. Killinger, L. Lusvarghi, A. Sola, Deposition mechanisms in high velocity suspension spraying: case study for two bioactive materials, Surf. Coat. Technol. 210 (2012) 28–45.

[54] E. Dongmo, R. Gadow, A. Killinger, M. Wenzelburger, Modeling of combustion as well as heat, mass, and momentum transfer during thermal spraying by HVOF and HVSFS, J. Therm. Spray Technol. 18 (5–6) (2009) 896–908.
[55] J.H.M. Goosen, A.J. Swieringa, J.G.M. Keet, C.C.P.M. Verheyen, Excellent results from proximally HA-coated femoral stems with a minimum of 6 years follow-up. A prospective evaluation of 100 patients, Acta Orthop. 76 (2) (2005) 190–197.
[56] L. Palm, S.-A. Jacobsson, I. Ivarsson, Hydroxyapatite coating improves 8- to 10-year performance of the link RS cementless femoral stem, J. Arthroplast. 17 (2) (2002) 172–175.
[57] T. Thierer, J.P. Davliakos, J. Daulton Keith Jr., J.J. Sanders, D.P. Tarnow, J.A. Rivers, Five-year prospective clinical evaluation of highly crystalline HA MP-1-coated dental implants, J. Oral Implantol. 34 (1) (2008) 39–46.
[58] W. Xue, X. Liu, X. Zheng, C. Ding, Effect of hydroxyapatite coating crystallinity on dissolution and osseointegration in vivo, J. Biomed. Mater. Res. A 74 (2005) 553–561.
[59] R.S. Lima, K.A. Khor, H. Li, P. Cheang, B.R. Marple, HVOF spraying of nanostructured hydroxyapatite for biomedical applications, Mater. Sci. Eng. A 396 (1–2) (2005) 181–187.
[60] R.B. Heimann, H.V. Tran, P. Hartmann, Laser-Raman and Nuclear Magnetic Resonance (NMR) studies on plasma-sprayed hydroxyapatite coatings: Influence of bioinert bond coats on phase composition and resorption kinetics in simulated body fluid, Materialwiss. Werkst. 34 (12) (2003) 1163–1169.
[61] I. Demnati, M. Parco, D. Grossin, I. Fagoaga, C. Drouet, G. Barykin, C. Combes, I. Braceras, S. Goncalves, C. Rey, Hydroxyapatite coating on titanium by a low energy plasma spraying mini-gun, Surf. Coat. Technol. 206 (2012) 2346–2353.
[62] Z. Yin, S. Tao, X. Zhou, C. Ding, Evaluating microhardness of plasma sprayed Al_2O_3 coatings using Vickers indentation technique, J. Phys. D. Appl. Phys. 40 (2007) 7090–7096.
[63] R. Gadow, A. Killinger, N. Stiegler, Hydroxyapatite coatings for biomedical applications deposited by different thermal spray techniques, Surf. Coat. Technol. 205 (4) (2010) 1157–1164.
[64] T. Kokubo, H. Takadama, How useful is SBF in predicting in vivo bone bioactivity? Biomaterials 27 (15) (2006) 2907–2915.
[65] A.L. Patterson, The Scherrer formula for X-ray particle size determination, Phys. Rev. 56 (15) (1939) 978–982.
[66] G. Bolelli, V. Cannillo, R. Gadow, A. Killinger, L. Lusvarghi, J. Rauch, M. Romagnoli, Effect of the suspension composition on the microstructural properties of high velocity suspension flame sprayed (HVSFS) Al_2O_3 coatings, Surf. Coat. Technol. 204 (8) (2010) 1163–1179.
[67] J. Fazilleau, C. Delbos, V. Rat, J.F. Coudert, P. Fauchais, B. Pateyron, Phenomena involved in suspension plasma spraying. Part 1: suspension injection and behavior, Plasma Chem. Plasma Process. 26 (2006) 371–391.
[68] C. Delbos, J. Fazilleau, V. Rat, J.F. Coudert, P. Fauchais, B. Pateyron, Phenomena involved in suspension plasma spraying. Part 2: Zirconia particle treatment and coating formation, Plasma Chem. Plasma Process. 26 (2006) 393–414.
[69] S. Basu, B.M. Cetegen, Modeling of liquid ceramic precursor droplets in a high velocity oxy-fuel flame jet, Acta Mater. 56 (12) (2008) 2750–2759.
[70] P. Kulkarni, P.A. Baron, K. Willeke, in: P. Kulkarni, P.A. Baron, K. Willeke (Eds.), Aerosol Measurement. Principles, Techniques, and applications, Third edition, J. Wiley & Sons Ltd., Chichester, UK, 2011, pp. 15–30.
[71] C. Qiu, Y. Chen, Manufacturing process of nanostructured alumina coatings by suspension plasma spraying, J. Therm. Spray Technol. 18 (2) (2009) 272–283.
[72] S. Dyshlovenko, B. Pateyron, L. Pawlowski, D. Murano, Numerical simulation of hydroxyapatite powder behaviour in plasma jet, Surf. Coat. Technol. 179 (1) (2004) 110–117.
[73] F.J. Krieger, Calculation of the viscosity of gas mixtures, U.S. Air Force Project RAND Research Memorandum, The RAND Corporation, Santa Monica, CA, USA, 1951. (Available on-line at http://www.rand.org/pubs/research_memoranda/2008/RM649.pdf (retrieved 29/08/2012)).
[74] E. Dongmo, A. Killinger, M. Wenzelburger, R. Gadow, Numerical approach and optimization of the combustion and gas dynamics in High Velocity Suspension Flame Spraying (HVSFS), Surf. Coat. Technol. 203 (15) (2009) 2139–2145.
[75] K. VanEvery, M.J.M. Krane, R.W. Trice, H. Wang, W. Porter, M. Besser, D. Sordelet, J. Ilavsky, J. Almer, Column formation in suspension plasma-sprayed coatings and resultant thermal properties, J. Therm. Spray Technol. 20 (4) (2011) 817–828.
[76] H. Podlesak, L. Pawlowski, R. d'Haese, J. Laureyns, T. Lampke, S. Bellayer, Advanced microstructural study of suspension plasma sprayed hydroxyapatite coatings, J. Therm. Spray Technol. 19 (3) (2010) 657–664.
[77] A. Antonakosa, E. Liarokapisa, T. Leventouri, Micro-Raman and FTIR studies of synthetic and natural apatites, Biomaterials 28 (2007) 3043–3054.
[78] R. Cuscó, F. Guitián, S. de Aza, L. Artús, Differentiation between hydroxyapatite and β-tricalcium phosphate by means of μ-Raman spectroscopy, J. Eur. Ceram. Soc. 18 (1998) 1301–1305.
[79] M.B. Volf, Mathematical Approach to Glass, Elsevier, The Netherlands, 1988.
[80] K.A. Gross, V. Gross, C.C. Berndt, Thermal analysis of amorphous phases in hydroxyapatite coatings, J. Am. Ceram. Soc. 81 (1) (1998) 106–112.
[81] C.F. Feng, K.A. Khor, E.J. Liu, P. Cheang, Phase transformations in plasma sprayed hydroxyapatite coatings, Scripta Mater. 42 (2000) 103–109.
[82] H. Füredi-Milhofer, V. Hlady, F.S. Baker, R.A. Beebe, N. Wolejko Wikholm, J.S. Kittelberger, Temperature-programmed dehydration of hydroxyapatite, J. Colloid Interface Sci. 70 (1) (1979) 1–9.
[83] H. Owada, K. Ymashita, T. Kanazawa, High-temperature stability of hydroxyl ions in yttrium-substituted oxyhydroxyapatites, J. Mater. Sci. Lett. 10 (1) (1991) 26–28.
[84] Y.S. Touloukian, C.Y. Ho, Thermophysical Properties of Matter: The TPRC Data Series, Plenum Publishing Company Limited, New York, NY, USA, 1970.
[85] R. McPherson, A model for the thermal conductivity of plasma-sprayed ceramic coatings, Thin Solid Films 112 (1984) 89–95.
[86] O. Babushkin, T. Lindback, A. Holmgren, J. Li, L. Hermansson, Thermal expansion of hot isostatically pressed hydroxyapatite, J. Mater. Chem. 4 (3) (1994) 413–415.
[87] C. Chu, J. Zhu, Z. Yin, P. Lin, Optimal design and fabrication of hydroxyapatite–Ti asymmetrical functionally graded biomaterial, Mater. Sci. Eng. A 348 (1–2) (2003) 244–250.
[88] K.P. Sanosh, M.-C. Chu, A. Balakrishnan, T.N. Kim, S.-J. Cho, Pressureless sintering of nanocrystalline hydroxyapatite at different temperatures, Met. Mater. Int. 16 (4) (2010) 605–611.
[89] S. Ramesh, K.L. Aw, R. Tolouei, M. Amiriyan, C.Y. Tan, M. Hamdi, J. Purbolaksono, M.A. Hassan, W.D. Teng, Sintering properties of hydroxyapatite powders prepared using different methods, Ceram. Int. 39 (1) (2013) 111–119.
[90] S. Saber-Samandari, K.A. Gross, Amorphous calcium phosphate offers improved crack resistance: a design feature from nature? Acta Biomater. 7 (2011) 4235–4241.
[91] X. Fan, E.D. Case, F. Ren, Y. Shu, M.J. Baumann, Part II: Fracture strength and elastic modulus as a function of porosity for hydroxyapatite and other brittle materials, J. Mech. Behav. Biomed. Mater. 8 (2012) 99–110.
[92] S.W.K. Kweh, K.A. Khor, P. Cheang, Plasma-sprayed hydroxyapatite (HA) coatings with flame-spheroidized feedstock: microstructure and mechanical properties, Biomaterials 21 (2000) 1223–1234.
[93] K.A. Khor, H. Li, P. Cheang, Significance of melt-fraction in HVOF-sprayed hydroxyapatite particles, splats and coatings, Biomaterials 25 (2004) 1177–1186.
[94] C.-W. Yang, T.-M. Lee, T.-S. Lui, E. Chang, Effect of post vacuum heating on the microstructural feature and bonding strength of plasma-sprayed hydroxyapatite coatings, Mater. Sci. Eng. C 26 (2006) 1395–1400.
[95] S. Yang, H.C. Man, W. Xing, X. Zheng, Adhesion strength of plasma-sprayed hydroxyapatite coatings on laser gas-nitrided pure titanium, Surf. Coat. Technol. 203 (2009) 3116–3122.
[96] C. Renghini, E. Girardin, A.S. Fomin, A. Manescu, A. Sabbioni, S.M. Barinov, V.S. Komlev, G. Albertini, F. Fiori, Plasma sprayed hydroxyapatite coatings from nanostructured granules, Mater. Sci. Eng. B 152 (2008) 86–90.
[97] J. Nohava, B. Bonferroni, G. Bolelli, L. Lusvarghi, Interesting aspects of indentation and scratch methods for characterization of thermally-sprayed coatings, Surf. Coat. Technol. 205 (4) (2010) 1127–1131.
[98] S.W.K. Kweh, K.A. Khor, P. Cheang, An in vitro investigation of plasma sprayed hydroxyapatite (HA) coatings produced with flame-spheroidized feedstock, Biomaterials 23 (2002) 775–785.
[99] K.A. Gross, S. Saber-Samandari, K.S. Heemann, Evaluation of commercial implants with Na91noindentation defines future development needs for hydroxyapatite coatings, J. Biomed. Mater. Res. B Appl. Biomater. 93 (2010) 1–8.
[100] R. Ahmed, N.H. Faisal, A.M. Paradowska, M.E. Fitzpatrick, K.A. Khor, Neutron diffraction residual strain measurements in nanostructured hydroxyapatite coatings for orthopaedic implants, J. Mech. Behav. Biomed. Mater. (2011) 2043–2054.
[101] P. Ostojic, C.C. Berndt, The variability in strength of thermally sprayed coatings, Surf. Coat. Technol. 34 (1988) 43–50.
[102] C.-W. Yang, T.-S. Lui, Effect of crystallization on the bonding strength and failures of plasma-sprayed hydroxyapatite, Mater. Trans. 48 (2) (2007) 211–218.
[103] C.-W. Yang, T.-S. Lui, Microstructural self-healing effect of hydrothermal crystallization on bonding strength and failure mechanism of hydroxyapatite coatings, J. Eur. Ceram. Soc. 28 (2008) 2151–2159.
[104] R.S. Lima, B.R. Marple, High Weibull modulus HVOF titania coatings, J. Therm. Spray Technol. 12 (2) (2003) 240–249.
[105] H.-M. Kim, T. Himeno, T. Kokubo, T. Nakamura, Process and kinetics of bonelike apatite formation on sintered hydroxyapatite in a simulated body fluid, Biomaterials 26 (2005) 4366–4373.
[106] S.-W. Ha, R. Reber, K.-L. Eckert, M. Petitmermet, J. Mayer, E. Wintermantel, Chemical and morphological changes of vacuum-plasma-sprayed hydroxyapatite coatings during immersion in simulated physiological solutions, J. Am. Ceram. Soc. 81 (1) (1998) 81–88.
[107] L. Sun, C.C. Berndt, K.A. Khor, H.N. Cheang, K.A. Gross, Surface characteristics and dissolution behavior of plasma-sprayed hydroxyapatite coating, J. Biomed. Mater. Res. 62 (2002) 228–236.
[108] R.B. Heimann, Characterization of as-plasma-sprayed and incubated hydroxyapatite coatings with high resolution techniques, Mater.-wiss. Werkstofftech. 40 (1–2) (2009) 23–30.
[109] Y.C. Tsui, C. Doyle, T.W. Clyne, Plasma sprayed hydroxyapatite coatings on titanium substrates. Part 2: optimisation of coating properties, Biomaterials 19 (1998) 2031–2043.
[110] C.M. Botelho, M.A. Lopes, I.R. Gibson, S.M. Best, J.D. Santos, Structural analysis of Si-substituted hydroxyapatite: zeta potential and X-ray photoelectron spectroscopy, J. Mater. Sci. Mater. Med. 13 (2002) 1123–1127.
[111] W. Janusz, E. Skwarek, The study of the properties of the hydroxyapatite/electrolyte interface, Ann. Univ. Mariae Curie-Skłodowska 64 (1) (2010) 11–20.
[112] N. Puvvada, P. Kumar Panigrahi, A. Pathak, Room temperature synthesis of highly hemocompatible hydroxyapatite, study of their physical properties and spectroscopic correlation of particle size, Nanoscale 2 (2010) 2631–2638.